

Master's Thesis

Measurement of the modulation transfer function of a digital radiographic system in consideration of object motion

Katharina Loot

Supervisor:
Dr. Andreas Block

Second advisor:
Prof. Dr. Georg Pretzler

January 2014

Institut für
Medizinische Strahlenphysik und Strahlenschutz
Klinikum Dortmund

Heinrich-Heine-Universität Düsseldorf

Contents

1. Introduction	4
2. The modulation transfer function	5
2.1. Contrast and the modulation transfer function	5
2.2. Imaging in the frequency domain	9
2.3. The modulation transfer function in digital radiography	12
2.3.1. Geometric Unsharpness	14
2.3.2. Diffraction	16
2.3.3. Sampling and Aliasing	17
2.3.4. Object Motion	18
3. The radiographic imaging system	22
3.1. Instrumentation and image formation	22
3.2. Interaction processes of X-ray radiation	24
4. Material and Methods for Measurement of the MTF	25
4.1. Radiation Quality	25
4.2. Test Device	25
4.3. Geometry	26
4.4. Measurement of the Conversion Function	26
4.5. Irradiation for determination of the MTF	28
4.6. Corrections of Raw Data	28
4.7. Motion Simulator	28
5. Analysis Technique	29
5.1. Preparation of the image data	30
5.2. Determination of the edge angle	31
5.3. Construction of the oversampled ESF	33
5.4. Derivation of the oversampled LSF	33
5.5. Fourier transform to obtain presampled MTF	35
5.6. Corrections	36
6. Results from Simulation	37
6.1. Analysis of Phase Errors	38
6.2. Reducing noise in the MTF	42
6.2.1. Smoothing	43

6.2.2. Averaging using several layers of data	47
6.3. Sampling and Aliasing	48
6.4. Motion Blur	51
6.4.1. Implementing uniform linear motion	51
6.4.2. Interaction between sampling aperture and motion	52
6.4.3. Restoration of motion-blurred images	53
7. Results from Experiments	60
7.1. Detector Response	60
7.2. Geometric Unsharpness	61
7.3. Motion Blur	63
7.4. Restoration	64
8. Conclusion	66
A. Mathematica code	68
A.1. MTF evaluation program	68
A.2. Noise reduction	71
A.3. Simulation images	72
Bibliography	74

1. Introduction

The modulation transfer function describes the resolution properties of imaging systems. It is a commonly used metric for the analysis of optical and electro-optical systems, especially if several subsystems are present.

Measurement of the modulation transfer function is part of the quality assurance for clinical radiography systems. With the changeover from analog screen-film systems to discrete digital systems, a novel analysis technique was required. By now, there exists a recommendation for measurement of the modulation transfer function of the detector [62203]. Other system components have not yet been conclusively examined. However, in many articles, the performance of the detector is falsely suggested to be representative for the performance of the entire imaging system.

In digital radiology, the patient is generally asked to refrain from breathing during the exposure. This minimizes motion artifacts sufficiently so that they have negligible influence on the image quality. However, there are patients who are unable to control their breathing or their limb movements, such as patients in intensive care or babies.

While post-processing in form of unsharp masking, look-up tables or spatial frequency filtering is typically available to the radiologist, no corrections for motion blur are available up until now. On the other hand, motion blur restoration is extensively used in photography and other optical systems which suffer from relative motion between object and imager. The question arises, whether motion blur restoration techniques from optical imaging systems can be transferred to digital radiography and which role the modulation transfer function could play in this idea.

As a first approach to this entirely new field, this thesis presents a comprehensive description of the modulation transfer function in digital radiography with special emphasis on the influence of object motion. The subject is examined both from the analytical and the experimental side. With further knowledge of the influence of motion on image degradation, it might be possible to restore blurred images, e.g. by implementing respiration curves of patients.

Starting off with a mathematical treatment of transfer functions, the frequency response of the most important subsystems is calculated from system properties wherever possible (chapter 2). After a short description of radiographic imaging systems and the measurement method in chapter 3 and 4, the analysis technique for derivation of the detector modulation transfer function is discussed at length in chapter 5. The technique is implemented in an evaluation program written in Mathematica. By use of simulation images, weak spots of the evaluation program are examined in detail (chapter 6). Furthermore, the behavior of the radiography system is predicted and compared to the experimental results in chapter 7. The thesis is closed with a summary and an outlook to future work.

2. The modulation transfer function

An imaging system creates a representation of an object. As this representation will not be perfect, measuring the kind and amount of alteration during the imaging process, in other words, the *image quality*, is crucial for developers and users of imaging systems. Our main objective is to find a mathematical description for the impact of object motion on image quality. However, there is no all-encompassing definition of image quality. The term depends on the imaging modalities and has subjective aspects. In medical imaging, the image quality describes the ability to provide an accurate diagnosis by means of the optical system. Some features of image quality that can be measured are the following: A satisfactory *contrast* will provide the ability to differentiate between structures with similar densities, the image can be corrupted by more or less *noise*, the *spatial resolution* of the system determines the amount of image detail and there exists a wide variety of *image artifacts*. Corresponding to this list, there exist numerous methods to measure one or more of the above aspects. For radiography in particular, there are comparatively simple experimental methods like measuring the resolution limit or the *signal-to-noise ratio*, and more sophisticated approaches like the *modulation transfer function* and the *detective quantum efficiency*. Which way is the most promising for our objective?

One can imagine that there have already been made some approaches on how to deal with motion blurred images in optical engineering. Such considerations are of great importance for analyzing the effects of digital and optical image stabilization in digital cameras, where hand tremors induce blurring [CKS⁺08], for the development of aerial survey lens systems, where the camera itself is in motion [LT88] and for correcting translational and rotational motion artifacts in magnetic resonance imaging or positron emission tomography [LWS05]. A literature survey of these fields shows, that the modulation transfer function is considered the most convenient tool for describing degradation in image quality caused by object motion.

In this chapter we will discuss mathematical and conceptual aspects of the modulation transfer function.

2.1. Contrast and the modulation transfer function

Contrast and spatial resolution are not independent of each other, as it might appear on first sight. Fig. 2.1 shows the image of a square wave grating that was taken with an X-ray unit at the Klinikum Dortmund. As the lines draw closer together, the contrast decreases until nothing but indistinguishable shades of gray are left. Thus the image detail (or spatial resolution) is limited by the contrast.

The term *contrast* describes a subjective visual perception and is familiar from photography. It refers to the range of distinctive shades of gray between the brightest and the darkest part of an object [Wil02]. Several approaches have been made to mathematically define contrast. We will see that there is no conclusive concept for all applications but that the image pattern itself determines the appropriate contrast definition.

In order to quantize contrast, we first need to find an expression for the brightness of an object. The photometric measure of brightness is called (*photon*) *flux density* or *luminance* and is defined as the amount of photon flux passing through a surface per unit of surface area [Wil02]. We will use the term flux density and identify it with the symbol \mathcal{W} .

Let us first consider a small single object of uniform flux density against a uniform background, as sketched in Fig. 2.2a. An observer will be adapted to the background and perceive the object as a change in flux density compared to the background. This is called *Weber contrast* and can be written as

$$C = \frac{\mathcal{W}_{\text{obj}} - \mathcal{W}_{\text{bg}}}{\mathcal{W}_{\text{bg}}}, \quad (2.1)$$

where \mathcal{W}_{obj} and \mathcal{W}_{bg} denote the flux densities of the object and the background [Pel90]. The Weber contrast takes values from -1 to ∞ . A negative value corresponds to a bright object on a dark background, a positive value occurs if the background is darker than the object.



Figure 2.2.: a) Small, single object in front of uniform background, suited for Weber contrast. b) Pattern without distinctive background, suited for Michelson contrast.

On the other hand, a periodic pattern like the one in Fig. 2.2b has no distinctive background. An observer will instead be adapted to the sum of minimal and maximal flux density

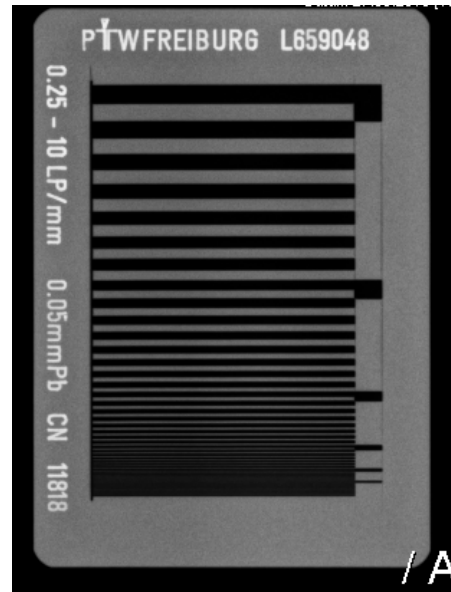


Figure 2.1.: CR image of a square wave grating with spatial frequencies in the range of 0.25-10 Lp/mm.

$(\mathcal{W}_{\min}, \mathcal{W}_{\max})$. This pattern can better be described by the *Michelson contrast* [Pel90]

$$C = \frac{\mathcal{W}_{\max} - \mathcal{W}_{\min}}{\mathcal{W}_{\max} + \mathcal{W}_{\min}} \quad (2.2)$$

and is also known as contrast modulation or simply *modulation*. It ranges from 0 (uniform flux density) to 1 (object features areas where flux density equals zero).

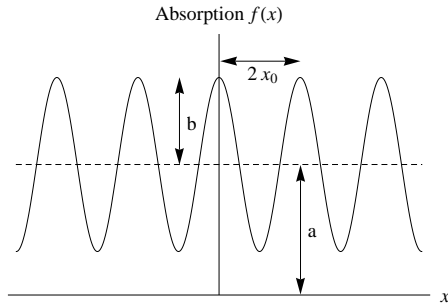


Figure 2.3.: Absorption distribution of a sinusoidal grating.

Sine wave grating. As a first illustration, we will now analyze the contrast of an object that has a sinusoidal flux density distribution. Imagine for example a radiography system, where the distribution can be generated by use of a sine wave grating, e.g. lead foil embedded in acrylic. To mathematically describe the object, we express the absorption of x-rays by the grating in the form

$$f(x) = a + b \cos(2\pi\omega x), \quad (2.3)$$

displayed in Fig. 2.3. The absorption varies along the distance x with a period of $T = 2x_0$, therefore $\omega = \frac{1}{T} = \frac{1}{2x_0}$ is called the spatial frequency, measured in m^{-1} . (Note: In a different context, ω often denotes the angular frequency with $\omega = 2\pi f = \frac{2\pi}{T}$. This does not apply here.) It is evident that for the contrast of this object the Michelson formula applies. (2.2) reduces to

$$C = \frac{\mathcal{W}_{\max} - \mathcal{W}_{\min}}{\mathcal{W}_{\max} + \mathcal{W}_{\min}} = \frac{(a + b) - (a - b)}{(a + b) + (a - b)} = \frac{b}{a}. \quad (2.4)$$

Any optical system will image a sinusoidal pattern in such a way that the wave form of the object is maintained. The reason for this can be found in a closer examination of convolution theory [Wil02]. For now, we simply assume its validity. The light flux in the image (denoted by primed values) will then be of the form

$$f'(x') = a' + b' \cos(2\pi\omega' x'). \quad (2.5)$$

The wave form remains, albeit frequency, amplitude and offset may vary and the distribution can be modified by a phase shift ϕ . x' is the variable of distance in the coordinates of the image. To describe the transfer of the flux distribution from object to image, one needs to consider the changes in a , b and ω (or x_0) and the addition of ϕ . Alternatively, we can express this transfer in quantities that are intuitively more accessible. The contrast in the image is $C' = b'/a'$, so the contrast transfer is the ratio

$$T_C = \frac{C'}{C} = \frac{b' \cdot a}{a' \cdot b}. \quad (2.6)$$

Considering an arbitrary object, the flux density distribution, being much more complicated, would be written as a Fourier series with individual parameters a_ω, b_ω for each occurring frequency ω . This implies that the contrast transfer T_C is generally a function of ω . It is called the *modulation transfer function* (MTF) $T(\omega)$ [Wil02].

Optical transfer function. The phase difference between object and image is also frequency-dependent. It is called the phase transfer function (PTF) and is mostly used to determine potential aberrations [Bor01]. To visualize how a phase shift effects the image, a spoke target (or *Siemens star*) can be imaged (Fig. 2.4). It consists of radial spokes so that the spatial frequency of adjacent spokes increases towards the center. A close look at the detail reveals a phase shift of π over a certain frequency range, indicated by the transition from white to black spokes and vice versa.

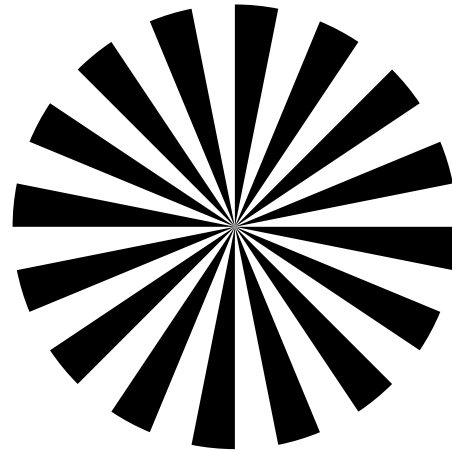


Figure 2.4.: A spoke target (Siemens star) is used to visualize phase shift in the image. [Wim]

The combination of modulation transfer function and phase transfer function is called the *optical transfer function* (OTF)

$$\text{OTF}(\omega) = T(\omega) \cdot e^{i\phi}. \quad (2.7)$$

It gives a complete description of the modifications that the flux density distribution undergoes during the imaging process.

Following this intuitive explanation, it is now time for a conceptual change; we will give the modulation transfer function a mathematical formulation.

2.2. Imaging in the frequency domain

Ideally, the image of this point source would again be an infinitely small point, its light flux density distribution in the form of a sharp peak. In the experiment, this will not be the case. Based on several factors (diffraction, imperfections of individual components, aberrations, etc.) it will resemble a more or less extended mound (Fig. 2.5). This image of a point source is called the *point spread function* (PSF) [Wil02] and will hence be written as $PSF(x, y)$. For a better understanding of the principles of imaging, we will first consider the imaging of a point source by an arbitrary optical system.

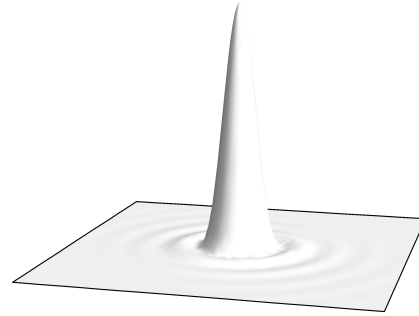


Figure 2.5.: Computer-generated plot showing the point spread function of a diffraction-limited system.

The transition from object to image is mediated by the *impulse response* $h(x, y)$ of the system. If we assume that the imaging process can be represented by a convolution operation, the impulse response of the optical system with unit magnification would relate the object $obj(x, y)$ to the image $im(x, y)$ via

$$im(x, y) = obj(x, y) * h(x, y) = \int_{-\infty}^{\infty} \int_{-\infty}^{\infty} obj(x', y') h(x - x', y - y') dx' dy', \quad (2.8)$$

where $*$ denotes the convolution. The above assumption requires the system to be linear and shift-invariant [Bor01]. Especially for sampled imaging systems this is not necessarily fulfilled, as will be discussed in later sections.

Fig. 2.6 visualizes the convolution operation: The object is finely sampled into single points. The system responds to every point with its impulse response, the point spread function. The superposition of these point images gives the final image of the object. In the case of a point source, the object would be described by a two-dimensional Delta distribution $\delta(x, y)$ so that $im(x, y) = h(x, y)$. It follows that the point spread function is equivalent to the impulse response

$$h(x, y) = PSF(x, y). \quad (2.9)$$

As $PSF(x, y)$ describes a density distribution, we assume the total light flux emanating from the point source to be unity, generating

$$\int_{-\infty}^{\infty} \int_{-\infty}^{\infty} PSF(x, y) dx dy = 1. \quad (2.10)$$

In general, the value of a point spread function decreases rapidly with distance from the ideal point image position and the limits can be reduced to the limits of the optical system.

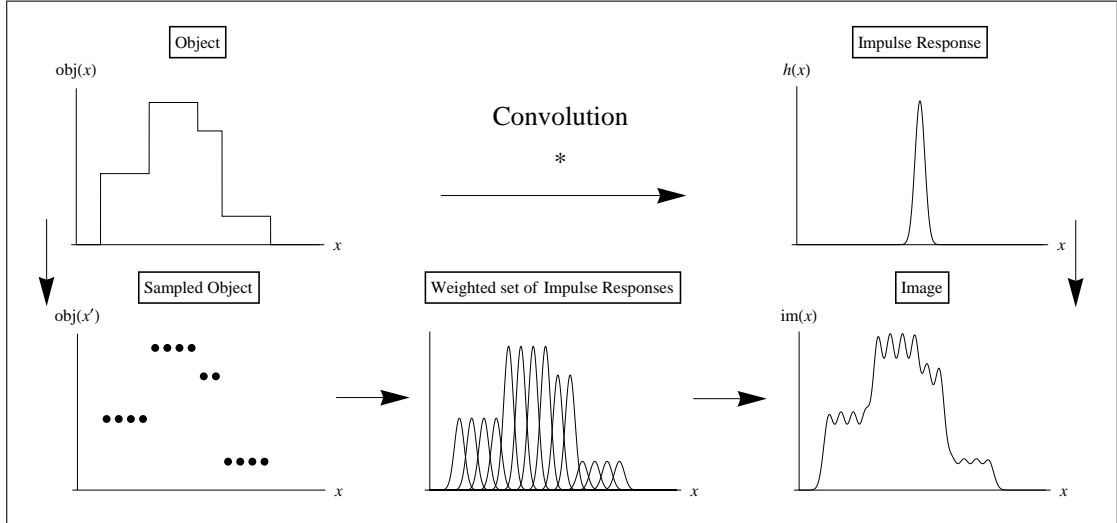


Figure 2.6.: Convolution in the imaging process.

In PSF measurement, the result generally contains contributions from several steps along the imaging chain, e.g. scattering, detector footprint. It is assumed that each step has its own PSF which combines with the others via convolution [Bor01], so the overall PSF is given by

$$\text{PSF}(x, y) = \text{PSF}_1(x, y) * \text{PSF}_2(x, y) * \dots \quad (2.11)$$

When discussing the response of an optical system, it is convenient to use the Fourier transforms of $obj(x, y)$, $im(x, y)$ and $h(x, y)$: $OBJ(\xi, \eta)$, $IM(\xi, \eta)$ and $H(\xi, \eta)$. This does not generate any new information, but allows additional insight into the behavior of the imaging system. The convolution theorem yields that the imaging process is now a simple multiplication [Bor01]:

$$IM(\xi, \eta) = OBJ(\xi, \eta) \cdot H(\xi, \eta). \quad (2.12)$$

$H(\xi, \eta)$ represents the spectrum of the impulse response and can be identified as the *optical transfer function* (OTF) which we encountered in (2.7) [Bor01]. From this follows the important result

$$\text{MTF}(\xi, \eta) = |H(\xi, \eta)| = |\mathcal{F}(\text{PSF}(x, y))|. \quad (2.13)$$

The spatial frequencies ξ and η are expressed in line pairs per mm lp/mm or in 1/mm with $1 \text{ lp/mm} = 1 \text{ 1/mm}$. Both units are frequently used in the literature. The MTF is normalized to have unit value at zero spatial frequency. It's course provides us with information on the ability of the system to maintain the contrast of the object for different spatial frequencies during the image process. In Fig. 2.7 we see the MTFs of two imaging systems A and B with differing performance. At the limiting resolution, the MTF falls below the threshold of the

noise-equivalent modulation (NEM), where the signal-to-noise-ratio is unity. System A has a lower limiting resolution, but the performance at mid-range frequencies is superior to that of System B. Note that the NEM is not necessarily constant, but can also be a function of spatial frequency. We can conclude that limiting resolution, though very convenient because a single-number performance criterion, can be misleading when comparing imaging systems. The MTF provides more complete performance information [Bor01].

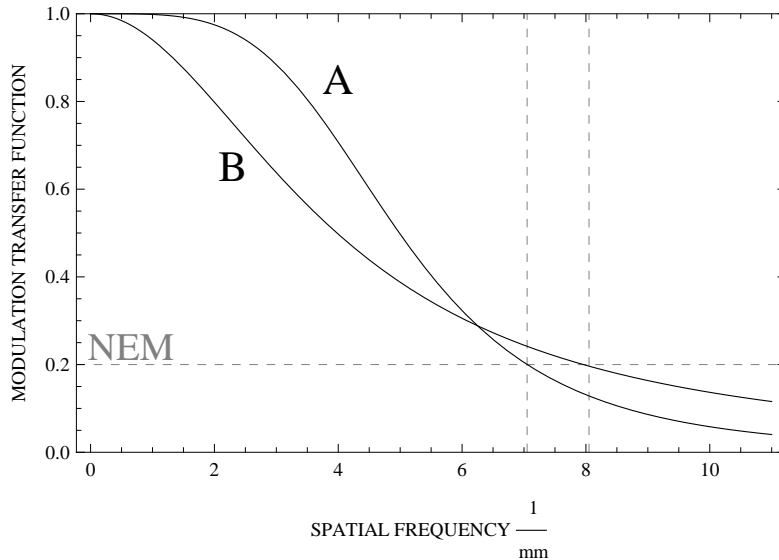


Figure 2.7.: Comparison of two systems A and B with reference to resolution. The MTF shows higher performance at midrange frequencies for system A in spite of a lower limiting resolution.

Line and edge spread function Analogous to the point spread function, the *line spread function* (LSF) is the distribution of the flux density in the image of a line source [Wil02]. The perfect line source has the flux distribution $obj(x, y) = \delta(x)1(y)$, its image is blurred due to imperfections in the optical system. Fig. 2.8 shows the intensity distribution in the image of a line source for a diffraction-limited system.

As the line source is constant along the y -axis, the LSF is only dependent on x :

$$LSF(x, y) = \delta(x)1(y) * PSF(x, y) \quad (2.14)$$

$$= \int_{-\infty}^{\infty} PSF(x, y') dy' = LSF(x). \quad (2.15)$$

The LSF can be interpreted as the line response of the optical system and used for calculation of its MTF [Bor01], as described by the relation in (2.16). Because the information is only contained in one direction, we only obtain a profile of the MTF:

$$|\mathcal{F}(\text{LSF}(x))| = \text{MTF}(\xi, 0). \quad (2.16)$$

However, reorienting the line source leads to different profiles which can be combined to give $\text{MTF}(\xi, \eta)$. As the LSF is easier to measure than the PSF, it is preferred when calculating the modulation transfer function from experimental data [Wil02].

Another elementary object to analyze is an illuminated edge object, mathematically described by a step function $\text{obj}(x, y) = \Theta(x)1(y)$. The image of this edge shows as a gradual transition from black to white. This is the *edge spread function* (ESF), sometimes referred to as *edge trace* [Bor01]. It is only dependent on x and expresses the superposition of line spread functions along the x -axis:

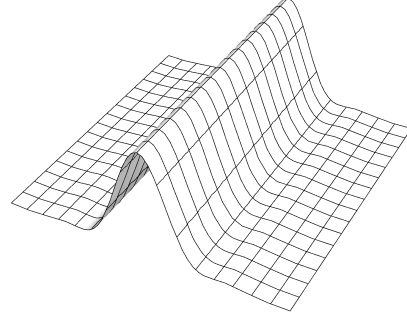


Figure 2.8.: Intensity distribution in the image, equivalent to the line spread function of the system.

$$\text{ESF}(x) = \Theta(x)1(y) * \text{PSF}(x, y) = \int_{-\infty}^x \text{LSF}(x')dx'. \quad (2.17)$$

If an edge object is used to experimentally determine the modulation transfer function, $\text{ESF}(x)$ will generally be transferred into $\text{LSF}(x)$ by differentiation

$$\frac{d}{dx} \text{ESF}(x) = \text{LSF}(x) \quad (2.18)$$

and subsequently Fourier transformed as in (2.16). We will present an edge analysis technique using exactly this derivation of the MTF from the ESF. Note that the MTF calculated from one edge image only represents a profile of the 2-dimensional $\text{MTF}(\xi, \eta)$ along the axis perpendicular to the edge. In the following, the term MTF always signifies a 1-dimensional profile $\text{MTF}(\xi)$.

2.3. The modulation transfer function in digital radiography

In the last chapter we derived the concept of the MTF for a general linear, shift-invariant system. We will now analyze the individual components that contribute to the MTF of a *digital radiographic imaging system*. Fig. 2.9 shows the components in the imaging chain that affect the resolution of a digital imaging system.

Starting from the object at hand, the first step is the actual image formation on the way from the object to the detector. Alteration of the image depends on the beam characteristics,

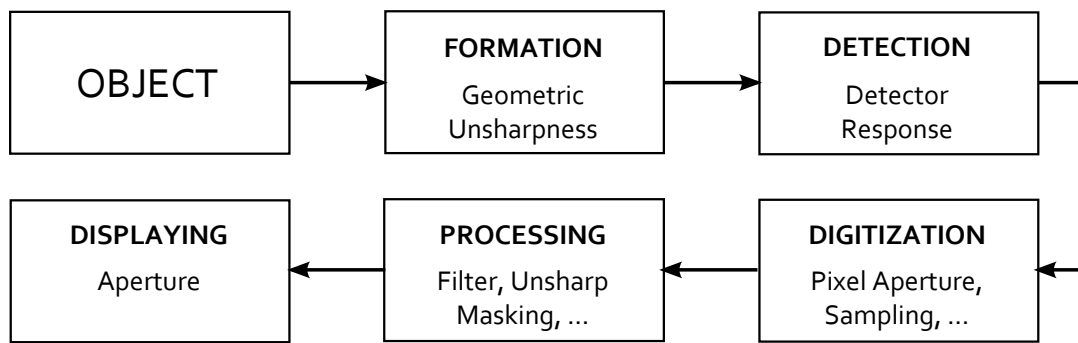


Figure 2.9.: The imaging process of a digital radiographic imaging system including possible influences on the MTF.

e.g. the size and shape of the focal spot and the magnification of the system. This is often described as the *geometric unsharpness* of the system. Next in the imaging chain comes the *detector response*, which contains information about light diffusion, scattering, etc. in the detector system. The transferred information up to this point forms the analog input for the digital system. Its MTF is the product of the MTF's for geometric unsharpness and detector response [GD84] and is labeled as MTF_A .

We have now reached the digitization of the image. The analog input is sampled and the image information is stored in the form of pixel values in a matrix. This step does not exist in analog systems, where the image is for example fixated on a (continuous) film, and it implicates several important changes. Firstly, the image is diffraction-limited by the *sampling aperture*. We already learned that this MTF component can be described as the Fourier transform of the sampling aperture, MTF_S . The product of MTF_A and MTF_S is called the *presampling* MTF of a digital imaging system, MTF_{PRS} , which describes the imaging process up to the sampling stage, including the diffraction caused by the sampling aperture, but excluding the effects of sampling itself [FTI⁺92].

Furthermore, the sampling distance (the distance between the centers of two adjacent pixels) limits the accuracy of the sampling process. One can easily imagine that a large sampling distance leads to a considerable loss of information. The characteristics of a signal that can be exactly sampled and the minimal sampling distance for this case will be described in the next section. For now, we record that the *digital* MTF includes the sampling stage and is denoted by the curved brackets in Eq. 2.19. It can be calculated by convolution of the presampled MTF with a comb function that depends on the sampling distances Δx and Δy in x - and y -direction [PSK84]. This is equivalent to multiplying the image with the comb function, generating a discrete output in the dimensions of the detector matrix.

If the image is filtered, this is expressed by the transfer function MTF_F of the filter. The last step in the image chain describes the response to the display aperture, expressed by MTF_D . The overall MTF can now be expressed by

$$\text{MTF}(u, v) = \left\{ \overbrace{[\text{MTF}_A(u, v) \cdot \text{MTF}_S(u, v)]}^{\text{MTF}_{\text{PRS}}} * \sum_{m=-\infty}^{+\infty} \sum_{n=-\infty}^{+\infty} \delta\left(u - \frac{m}{\Delta x}, y - \frac{n}{\Delta y}\right) \right\} \cdot \text{MTF}_F(u, v) \cdot \text{MTF}_D(u, v). \quad (2.19)$$

If the MTF is to be used for an imaging system analysis, it is convenient to develop MTF expressions for the various subsystems. This will also help us get further acquainted with the MTF. In this section, we take a closer look at some MTF components which play a role in radiographic imaging and discuss their relevance.

2.3.1. Geometric Unsharpness

The geometric unsharpness of the radiography system is caused by the finite size of the effective focal spot. It is also influenced by the shape of the effective focal spot and the magnification factor of the system [LR67]. An ideal effective focal spot would be infinitely small and project the object onto the detector, modified by the magnification. If the effective focal spot has a finite width, the image is blurred around the edges. This is illustrated in Fig. 2.10, where the edge of a radiopaque plate is used for analysis. Instead of a jump discontinuity between minimum and maximum intensity, a gradual transition over the width of U_g , the so-called *penumbra*, is detected. U_g can be calculated from the size f of the focal spot, the source-object distance d_1 and the object-detector distance d_2 :

$$U_g = f \cdot \frac{d_2}{d_1}. \quad (2.20)$$

U_g does not depend on the angle between the source-detector direction and the source-object direction. To calculate the component MTF_{g_u} that corresponds to the geometrical unsharpness, we interpret the detected intensity as the ESF (Fig. 2.11a). Differentiation yields the LSF (Fig. 2.11b), from which MTF_{g_u} is determined via Fourier transformation. The result is a sinc function [LR67]

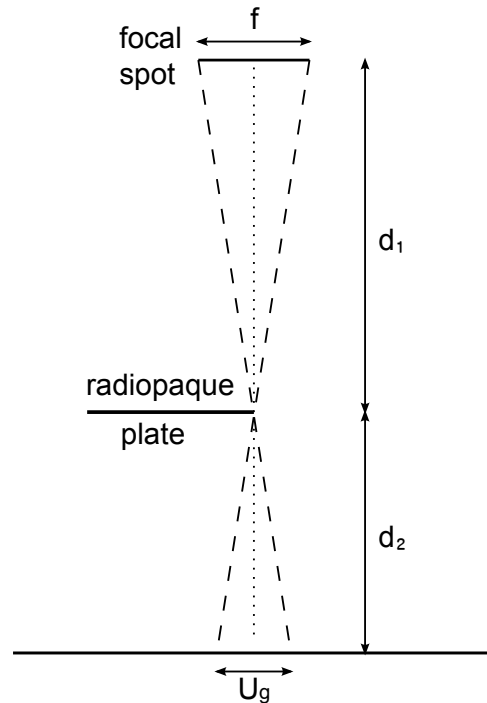


Figure 2.10.: Penumbra U_g generated by finite size of the focal spot.

$$MTF_{gu}(\xi) = \left| \text{sinc}(\pi\xi U_g) \right| = \left| \frac{\sin(\pi\xi U_g)}{\pi\xi U_g} \right| \quad (2.21)$$

as displayed in Fig. 2.11c

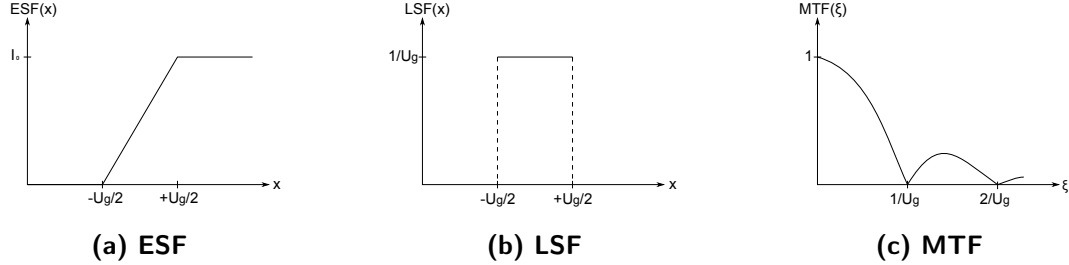


Figure 2.11.: Derivation of the MTF for geometrical unsharpness. (a) ESF(x) is equivalent to the intensity profile in the penumbra. (b) LSF(x) is obtained by differentiation of ESF(x). (c) Fourier transform yields MTF(ξ).

If the effective focal spot is non-uniform, U_g depends on x , y and MTF_{gu} differs in the various directions.

MTF_{gu} reaches the first zero at $\xi_0 = 1/U_g = d_1/(f \cdot d_2)$. To understand this drop in performance, imagine the radiologic object to be a grating with alternating sections of radiopaque and radiolucent material. At ξ_0 , the width U_g of the penumbra exactly equals the width of one linepair. The ESF is a continuity of triangle functions, leading to a LSF with alternating positive and negative values of the same modulus. The MTF_{gu} is then zero for all frequencies. For frequencies $\xi > \xi_0$, the penumbras start to overlap, thus creating sections in which the ESF is constant again. However, the intensities in these sections do not reach the original minimum and maximum values, so the modulation is significantly lower than before. The process continues for higher frequencies: The second zero is reached at $\xi = 2/U_g$, where U_g equals the width of two line pairs, and so on.

ξ_0 can be increased by reducing the size of the effective focal spot or positioning the object closer to the detector, resulting in an overall higher MTF_{gu} and therefore better image quality. The magnification factor m of the system can be expressed as $m = \frac{d_1+d_2}{d_1} = 1 + \frac{d_2}{d_1}$ and can thus be identified in the functionality of MTF_{gu} .

We calculate the first zero $\xi_0 = 1/U_g$ for realistic parameters in a clinical radiography system.

Geometry 1: $d_1=0.8$ m, $d_2=0.2$ m, $f=0.6$ mm

$$\frac{1}{U_g} = \frac{d_1}{f \cdot d_2} = 6.7 \frac{\text{Lp}}{\text{mm}}. \quad (2.22)$$

Geometry 2: $d_1=0.9$ m, $d_2=0.1$ m, $f=1.2$ mm

$$\frac{1}{U_g} = \frac{d_1}{f \cdot d_2} = 15 \frac{\text{Lp}}{\text{mm}}. \quad (2.23)$$

2.3.2. Diffraction

The diffraction MTF is of great importance in optical imaging. Unlike other influences, diffraction caused by the finite-sized aperture is inherent in the system and cannot be eliminated. The system with the best possible imaging performance is therefore called *diffraction-limited system* [Bor01]. For example, in optical systems with circular aperture and Fraunhofer diffraction one observes the so-called *Airy pattern*. In general, the theory of diffraction is rather complicated and can only be simplified for certain limiting cases. For a general calculation of the flux density distribution in an image, one employs the Huygens-Fresnel principle or its mathematical description, the Fresnel Kirchhoff integral formula. Detailed information on this can be found in [BW99].

Huygens stated that every point of a wave front is the origin of a new spherical wavelet and that the envelope of all wavelets forms the new wave front. To this Fresnel added the assumption that the wavelets interfere with each other. Later on, Kirchhoff provided a mathematical basis for this theory [BW99]. The *Fresnel-Kirchhoff formula* describes the light disturbance at one point P, caused by light of wavelength λ emerging from another point P' and propagating through an opening of size δ in a plane, opaque screen.

The Fresnel-Kirchhoff formula has two limiting cases for which the calculation can be simplified: If the distances between light source, aperture stop and detector are large, the curvatures of incident and diffracted waves are large enough for the waves to appear plane. This is called *Fraunhofer diffraction*. If the distances are small, the curvatures of the wave fronts are significant and the mathematical survey becomes more complicated [Fow75]. This is called *Fresnel diffraction*.

To distinguish between these cases, one uses the Fresnel number

$$F = \frac{\delta^2}{L\lambda} \quad (2.24)$$

$F \ll 1$: Fraunhofer diffraction

$F \approx 1$: Fresnel diffraction

λ is the wavelength, δ is the characteristic size of the aperture and L is either the distance between aperture and screen or the harmonic mean of the distances source - aperture and aperture - screen. For $F \gg 1$, the diffraction is neglectable and the system can be described with geometrical optics.

In the case of our radiography system, we can assume $\lambda = 10^{-11}$ m and $L = 0.3$ m. The resulting aperture sizes for the diffraction types are thus:

Fraunhofer diffraction	($F = 0.01$) :	$\delta \approx 10^{-7}$ m
Fresnel diffraction	($F = 1$) :	$\delta \approx 10^{-6}$ m
Geometrical optics	($F = 100$) :	$\delta \approx 10^{-5}$ m

The aperture opening of $\delta \approx 10^{-5}$ m corresponds to a spatial frequency of about 50 Lp/mm. This is way beyond the resolution of any radiographic system, as experiments show. We conclude

that diffraction phenomena do not have a primary influence on the imaging performance of a radiographic system.

2.3.3. Sampling and Aliasing

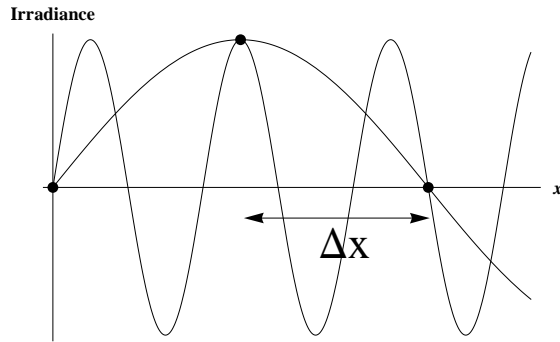


Figure 2.12.: Aliasing of high frequencies in digital imaging systems.

A sine wave is completely determined by its samples if more than two samples per cycle are taken. If Δ denotes the sampling distance, the critical spatial frequency is the Nyquist frequency at $\xi_{Ny} = \frac{1}{2\Delta}$ [PTVF07]. At this frequency, the samples can be the peak and trough values or, in the worst case, always the value of half the amplitude of the wave. For frequencies $\xi < \xi_{Ny}$, sampling will provide all values of the sine wave.

This has several important implications: If we sample a continuous function $h(t)$ that is bandwidth limited to frequencies $|\xi| < \xi_{Ny}$ at the sampling distance Δ , then $h(t)$ can

be expressed by the sum of its samples

$$h(t) = \Delta \sum_{n=-\infty}^{+\infty} h_n \frac{\sin(2\pi\xi_{Ny}(t - n\Delta))}{\pi(t - n\Delta)}, \quad (2.25)$$

where n is the number of the sample. This is known as the *sampling theorem* [PTVF07]. On the other hand: If the signal is undersampled as shown in Fig. 2.12, any frequency $|\xi| \geq \xi_{Ny}$ will be misinterpreted and fit into the region $-\xi_{Ny} < \xi < \xi_{Ny}$, generating higher contributions for certain frequencies. This effect is called *aliasing* [PTVF07].

In 2.2 we learned that the mathematical description of the imaging process by convolutional analysis requires the system to be shift-invariant. We consider the imaging of a thin line with a pixel array detector. If the line is orientated parallel to the pixel columns, the line can be centered on one pixel column or fall on two adjacent columns, thus rendering very different digital images. This shift variance generally forbids a transfer-function approach. However, if a generalized impulse response is introduced, the concept remains applicable [PSK84].

The finite size of the pixel detectors has implications on the system not unlike the ones for geometrical unsharpness. The MTF component is also a sinc function, the first zero appearing at $\xi_0 = \frac{1}{\Delta}$. We assume negligible dead space between adjacent pixels. Hence the terms *pixel aperture* and *pixel spacing* are equivalent. For the Siemens AXIOM Multix MT, the pixel spacing is 0.16 mm in both directions, causing a zero of the MTF at a spatial frequency of 6.25 Lp/mm. This result is close to the one for geometric unsharpness in (2.22), so these components have about the same amount of influence on the MTF. Note that the Nyquist frequency of the system is 3.125 Lp/mm, and that the calculated discrete MTF values

can be spurious above this frequency. If the pixel spacing does not equal the pixel aperture, the Nyquist frequency must be calculated via the pixel spacing, which denotes the sampling frequency, and the sampling PSF has the width of the pixel aperture.

As we will be primarily interested in the inherent resolution properties of the system, our methods will aim at measuring the presampled MTF, so that aliasing effects, processing and displaying of the image can be neglected.

2.3.4. Object Motion

A theoretical formulation of the OTF (and, thereby, MTF) component caused by object motion was developed in the 60s for simple types of motion. [Tro60] describes the effect on resolution caused by uniform velocity motion, parabolic motion, and high temporal frequency sinusoidal vibration. Expressing OTFs for arbitrary motion functions became of interest in the 90s. In reconnaissance, astronomy, machine vision and other imaging systems, the image degradation from motion was more severe than that from the electronics and optics. A thorough description of the influence of motion on the image quality was essential for efficiency control of stabilization systems, as well as the first step towards restoration of motion-blurred images.

A numerical calculation of the OTF for arbitrary motions was proposed in 1994 by Hadar et al [HDK94]. Three years later, Stern and Kopeika were able to obtain analytical expressions for the OTF by means of the statistical moments of the motion function [SK97]. This method is presented in the following.

We assume an arbitrary motion function $\chi(t)$ transverse to the optical axis. The effect of motion parallel to the optical axis will generally be much smaller and requires a different description, e.g. via modification of the geometric unsharpness. In the spatial domain, the image blur can be described with the PSF. More often than not, the motion will be in one direction only. The problem can then be confined to one dimension and we search for an expression of the LSF instead. In the experiment, we could determine the LSF by imaging a slit which is moved transversely to the optical axis during the exposure time. During the exposure, the detector would integrate the displacements of the slit, detecting higher exposure values at places where the slit passes more often. The motion of the slit can be described by the motion function $\chi(t)$. Alternatively, we can also use a histogram of $\chi(t)$, which records the frequency with which the slit occurs at a point $\chi(t)$. This histogram is called a *probability density function* (PDF), a term well known from probability theory. We observe that the PDF takes exactly the form of the LSF.

This transfer from probability theory will allow us to calculate the OTF from the motion function. We already know the relation between OTF and LSF:

$$\text{OTF}(\omega) = \mathcal{F}(\text{LSF}(x)) = \int_{-\infty}^{\infty} \text{LSF}(x) \exp(-i\omega x) dx. \quad (2.26)$$

In this definition, ω is the spatial angular frequency, not to be confused with the spatial frequency $\xi = \omega/2\pi$. The LSF is absolutely integrable ($\int_{-\infty}^{\infty} |\text{LSF}(x)| dx = 1$) and nonzero

over a finite interval. Therefore, the OTF is analytical and can be expressed in form of a Taylor series:

$$\text{OTF}(\omega) = \sum_{n=0}^{\infty} \frac{1}{n!} \left. \frac{\partial^n \text{OTF}(\omega)}{\partial \omega^n} \right|_{\omega=0} \omega^n. \quad (2.27)$$

We can calculate the n -th derivative of the OTF at zero spatial frequency from the LSF using (2.26):

$$\left. \frac{\partial^n \text{OTF}(\omega)}{\partial \omega^n} \right|_{\omega=0} = \frac{\partial^n}{\partial \omega^n} \int_{-\infty}^{\infty} \text{LSF}(x) \exp(-i\omega x) dx \Big|_{\omega=0} = (-i)^n \int_{-\infty}^{\infty} x^n \text{LSF}(x) dx. \quad (2.28)$$

With the interpretation of $\text{LSF}(x)$ as the PDF, the integral can be identified as the n -th moment $m_n = E(x^n)$ of the motion function. Drawing further on probability theory (details in [Pap84]), we now perform the transition from spatial to time domain, using the time PDF $f_t(t) = \frac{1}{\tau} \Theta(t - t_0) \Theta((t_0 + \tau) - t)$. t_0 indicates the beginning of the exposure and τ is the exposure duration. The n -th moment can now be written as

$$m_n = E(x^n) = \int_{-\infty}^{\infty} x^n(t) f_t(t) dt = \frac{1}{\tau} \int_{t_0}^{t_0+\tau} x^n(t) dt. \quad (2.29)$$

We insert these expressions into (2.27) and obtain the final result

$$\text{OTF}(\omega) = \sum_{n=0}^{\infty} \frac{m_n}{n!} (-i\omega)^n, \quad (2.30)$$

$$m_n = \frac{1}{\tau} \int_{t_0}^{t_0+\tau} x^n(t) dt. \quad (2.31)$$

When the motion is symmetrical around the $x = 0$ axis, all odd moments are zero and the OTF is real. The relation between the motion function and the OTF (2.30) is not linear. The OTF of a combination of two motion functions therefore cannot be calculated by cascading the OTFs of the individual motion functions.

Sometimes, only samples x_i of the motion function are known. In these cases, the moments are calculated from the samples via

$$m_n = \frac{1}{S} \sum x_i^n, \quad i = 1, \dots, S. \quad (2.32)$$

The infinite sum in (2.30) reduces to a closed expression only for special cases, like uniform velocity motion. In general, the sum is truncated at N -th order, which induces an approximation error of

$$|\text{Err}(N)| \leq \frac{\omega^{N+1}}{(N+1)!} \mu_{N+1}, \quad \mu_k = \frac{1}{\tau} \int_{t_0}^{t_0+\tau} |\chi(t)|^k dt. \quad (2.33)$$

μ_k is the k -th order absolute moment. Motion functions which only differ in an offset naturally produce the same OTF. However, the convergence is found to be better for centralized motions.

Uniform linear motion As an example, we will calculate the MTF for uniform linear motion from (2.30). The motion function shall be $\chi(t) = v \cdot t$, $t_0 < t < t_0 + \tau$, with v the constant velocity. We start by calculating the n -th moment of the motion function:

$$m_n(t_0; v, \tau) = \frac{1}{\tau} \int_{t_0}^{t_0+\tau} (vt)^n dt = \frac{v^n t^{n+1}}{\tau(n+1)} \Big|_{t_0}^{t_0+\tau}. \quad (2.34)$$

Substituting this into (2.30) and using the power series $\exp(x) = \sum_{n=0}^{\infty} \frac{x^n}{n!}$, the OTF takes the form

$$\text{OTF}(\omega) = \sum_{n=0}^{\infty} \frac{(v(t_0 + \tau))^{n+1} - (vt_0)^{n+1}}{v\tau(n+1)!} (-i\omega)^n \quad (2.35)$$

$$= \frac{\exp(-ivt_0\omega)}{-iv\tau\omega} (\exp(-iv\tau\omega) - 1) \quad (2.36)$$

$$= \frac{\exp(-iv(t_0 + \frac{\tau}{2})\omega)}{-iv\tau\omega} \cdot \left(\exp\left(\frac{-iv\tau\omega}{2}\right) - \exp\left(\frac{iv\tau\omega}{2}\right) \right) \quad (2.37)$$

$$= \text{sinc}\left(\frac{v\tau}{2}\omega\right) \cdot \exp\left(-iv\left(t_0 + \frac{\tau}{2}\right)\omega\right). \quad (2.38)$$

Converting ω into the spatial frequency ξ , we obtain the MTF

$$\text{MTF}(\omega) = |\text{OTF}(\omega)| = \left| \text{sinc}\left(\frac{d}{2}\omega\right) \right| = |\text{sinc}(\pi d\xi)|, \quad (2.39)$$

where $d = v \cdot \tau$ is the spatial extent of the blur. This expression is well known in the literature, as it can easily be calculated from the blur in the spatial domain. We will do so in 6.4.

The exposure time in projection radiography varies over a large range (1 ms to 1000 ms). As an example, let us consider a pediatric abdominal radiography with a short exposure time of 20 ms. If the pixel spacing of the detector is 0.16 mm, a uniform motion with a velocity of 2.4 cm/s already induces a blur of 3 px width. The system MTF is multiplied with the MTF component from motion, which is shown in Fig. 2.13. This forces the overall MTF to zero at 2.1 Lp/mm, greatly reducing the image resolution. The velocities during limb movements of children can be much higher, resulting in severe image degradations.

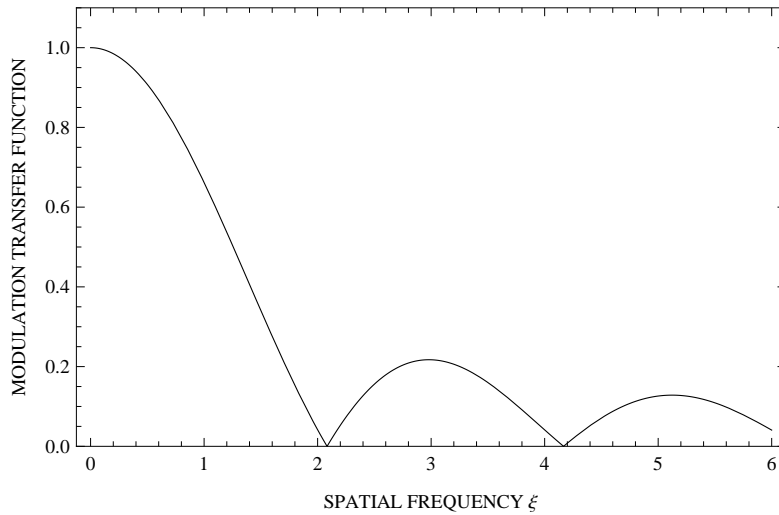


Figure 2.13.: Reduction of resolution in the imaging system by motion blur with an extent of $3 \text{ px} = 0.48 \text{ mm}$.

The method presented here is based on the knowledge of the motion function. However, in cases where the motion function is unknown, the MTF can still be approximated. In a motion-blurred image, the image characteristics along the direction of motion differ from the characteristics along other directions. Yitzhaky and Kopeika were the firsts to show, that it is possible to extract information about the velocity and the motion direction from the image itself, using motion-induced correlations between pixels [YK97]. Their work has progressed and is now known as *blind restoration*, combining the identification of blur parameters and their application in the restoration process.

3. The radiographic imaging system

Projection radiography is the oldest and most fundamental technique in medical imaging. It can be used to image almost every part of the human body and the chest x-ray is typically the most frequently performed examination in any hospital. Projection radiography creates image contrast by tissue-specific transmission of x-rays in the body. The three-dimensional body volume is projected onto a two-dimensional imaging surface. Therefore, the major limitation is the low depth resolution, as superimpositions of surrounding tissues may hide important lesions [PL06]. A schematic diagram of a conventional projection radiography system with all important features is shown in Fig. 3.1.

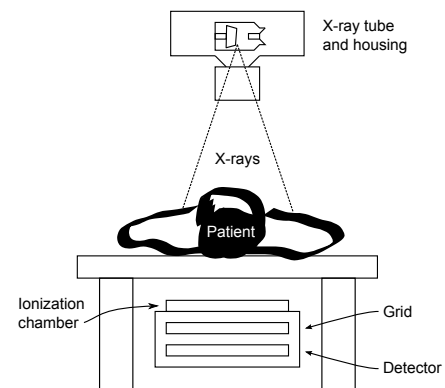


Figure 3.1.: Conventional projection radiographic system.

3.1. Instrumentation and image formation

The main features of a clinical radiography system are the X-ray tube, the image detector and patient positioning devices. Additional components include means of shaping or filtering the beam and a computer system.

Extensive information about the X-ray technique used in clinical imaging can be found in [PL06] and [Dös00]. We will content ourselves with a review based on these sources:

The X-ray tube basically contains a cathode and an anode in an evacuated glass tube. The cathode consists of a filament (e.g. crystalline tungsten) in a focusing cup. The electrons are boiled off the filament through *thermionic emission* and are then accelerated towards the anode. This tube current (mA) is in the range of 50 to 1200 mA. The acceleration is results from applying high voltages (ranging from 20 kVp up to 150 kVp) for a short period of time (around 0.1s). The focusing cup, a small depression in the cathode, causes the electrons to form a narrow beam that strikes only a small area of the anode, the *actual (electronic) focal spot*. The anode target is generally made out of molybdenum with a rhenium-allied tungsten coating. The incoming electrons are deflected by the static field of the tungsten atoms, producing *bremstrahlung*. Furthermore, the accelerated electrons can expel electrons from the inner shells of the tungsten atoms. The vacancies are filled by electrons from outer

shells. Their transitions cause cascaded emission of radiation with energies that correspond to the binding energies of the electrons. This is called *characteristic radiation*.

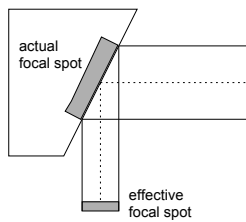


Figure 3.2.: Smaller effective focal spot with angled anode.

A major problem is the low conversion factor. Less than 1% of the electron energy produces X-ray radiation, the rest is converted into heat which can damage the anode. A high spatial resolution and improved heat dissipation are accomplished by angling the anode as in Fig. 3.2. The heat is dispersed over a greater area of the anode target, while the useful X-ray radiation (normal to the electron beam) appears to originate from a smaller *effective focal spot*. To further increase the heat dissipation, the anode is rotated so that an annular region is hit by the electrons. Typical values for the anode rotation are 3200 to 3600 rpm. The product of mA and exposure time defines the exposure (*mAs*). It is either controlled by a fixed timer or an automatic exposure control

(AEC). While the fixed timer regulates the chosen exposure time via a microprocessor and a silicon-controlled rectifier switch, the AEC circuitry determines the exposure time for the required mAs automatically with use of the ionization chambers between table and detector.

The image receptor in digital radiography is nowadays a flat panel detector. Its active matrix array consists of a great number of semiconductor elements that are deposited on a substrate. For *indirect receptors*, the active matrix array is coupled to an intensifying screen that contains phosphors. The X-ray radiation causes the phosphor atoms to emit light in the visible spectrum which is then detected by photodetectors. In the case of *direct receptors*, the array is coupled to a photoconductor. The X-rays directly induce an electric charge in the photoconductor (e.g. amorphous selenium) without the conversion to visible light. After exposure, the signal from each pixel is amplified and stored in the image memory of the digital image processor.

X-ray sources are polyenergetic. The energy distribution can be influenced by filtration of the beam. Low-energy x-ray photons do not contribute to the image, but to the patient dose, as they get completely absorbed by the body. The inherent filtering of the tube and the optional added filtering with metal slabs (generally aluminum) absorb low-energy photons before they reach the body. Thereby the energy spectrum is shifted to higher energies, which is called *beam hardening*. It is almost always sufficient to use only a part of the available x-ray beam for imaging. Therefore, the beam can be shaped by a collimator, which consists of movable pieces of lead that absorb the x-rays outside the desired field of view. A part of the photons which have passed through the body will be corrupted by scattering processes. A grid featuring lead strips is placed in front of the detector to absorb the off-axis photons. However, some photons of the primary beam are absorbed as well, which requires an overall higher exposure. The use of a grid is recommended for x-ray photon energies above 60 kVp or when imaging body parts thicker than 10 cm.

Our measurements will be performed at the Klinikum Dortmund with a digital radiography

system (Siemens Axiom Multix MT) that features a mobile full format flat panel detector. The image matrix consists of 2208 x 2688 px with detector dimensions of 35 cm x 43 cm. This size corresponds to the size of the largest film used in analog radiography systems. The detector can be inserted into the table tray or the detector wall stand. The pixel spacing is 0.16 mm in both horizontal and vertical direction. The inherent filtration consists of 0.2 mm aluminum.

3.2. Interaction processes of X-ray radiation

We now consider the most important interaction processes that take place in any radiological object during the exposition.

The first and most important process is the *photoelectric effect*. It is the dominant interaction at X-ray energies up to 1 MeV and is the primary way in which a contrast is developed in the image. The incoming X-ray photon collides with an inner shell electron. If its energy is greater than the electron binding energy, the electron can be ejected from the atom. It leaves a vacancy that will be filled by an electron from a higher shell, producing a fluorescent X-ray. Any X-ray photon that is absorbed can no longer reach the detector. This way, the absence of radiation creates the image. The interaction probability strongly depends on the X-ray energy E and the atomic number Z . If the X-ray photon is too energetic, the interaction probability decreases. The more tightly bound the electrons are (large Z), the greater the probability becomes. The interaction probability is approximately proportional to Z^3/E^3 . The dependency on the cube of the atomic number provides a great sensitivity to different tissues.

Another important process is *Compton scattering*. This is a scattering event in which the incoming X-ray photon collides with an outer-shell electron. The energy of the photon is thus reduced and its direction of flight altered. Although the Compton effect is dominant only for higher energies than those used in radiography, it is still of great importance in diagnostic imaging. The energy loss might be negligible, but the scattered X-ray photons are distributed quasi-isotropically. Deflected from their original path, they are either absorbed in the patient, adding to the radiation dose, or reach the detector where they give false information on their origin, creating a background noise that obscures the image. Thus, the image contrast is reduced.

The third process is *Thomson scattering*. This is the low-energy limit of Compton scattering, where the energy of the X-ray photon is unaltered and only the direction is changed. The photon causes oscillation of a free charged particle, which in its turn emits dipole radiation of the same frequency. Contrary to Compton scattering and the photoelectric effect, no ionization occurs.

4. Material and Methods for Measurement of the MTF

The method for obtaining the edge image is mainly based on the international standard IEC 62220-1 [62203], and the German equivalent DIN EN 62220-1:2005-01 [62205]. Deviations from these papers are clearly marked and discussed. The IEC 62220-1 specifies the methodology for measuring the DQE in a digital 2-D detector used for general radiography. This includes measurement of air kerma, the characteristic function and the MTF of the detector. It is applicable for any area detector, including the direct-conversion flat panel detector, which is part of our system. It is very important to note, that the above papers aim at measuring the *detector MTF only*. The measurement method does not allow for influences of geometric unsharpness or scattering, let alone object motion. It is therefore obvious that the above papers can only act as a suggestion and are not binding for our purpose, as our results will primarily be interesting in a qualitative analysis and will not be comparable to published MTF results which focus primarily on the detector MTF.

4.1. Radiation Quality

To facilitate comparison between determined characteristics for different imaging systems, IEC 62220-1 specifies 4 spectra (RQA 3,5,7, and 9) according to IEC 61267 [61205]. The spectra are determined by adjusting the kVp of the generator so that a specified half-value layer (HVL) is achieved for an equally specified thickness of the added Al filter. Of only one spectrum is used, it should be RQA 5 (added filtration 21 mm Al, HVL 7.1 mm Al).

As our results will not be comparable to literature for several reasons, it is not necessary to use the specified beam qualities. Instead, we followed the recommendation of Siemens to refrain from using more than 60 kVp for exposures without a strongly attenuating object in the beam path, as this might damage the detector. For all MTF measurements with the test device, we therefore used an x-ray beam quality of 60 kVp without additional filtration and a milliamperere seconds setting of 1.8 mAs.

4.2. Test Device

The images for MTF determination were acquired with an edge device. IEC 62220-1 suggests the use of a tungsten plate (thickness 1 mm) with a precision edge surrounded by lead (thickness

3 mm). This edge device is *opaque* to x-rays and features minimal secondary radiation from the test object itself. The lead frame improves the approximation of an infinitely long edge.

In the absence of a device with the above specifications, we used the edge of a lead foil test for analysis (PTW Freiburg, L659048). The device consists of 0.05 mm lead foil embedded in 2 mm acrylic. This corresponds to the translucent edge device used in former experiments by Samei et al., who also compared it to the opaque edge device [SRIC06]. From this work we know, that the MTF obtained with a *translucent* edge device is 0.7 % below the more accurate value obtained with an opaque edge device for the same beam quality (RQA 5) in the zero to cutoff frequency range. This is important to remember before interpreting the absolute MTF values. Furthermore, the usable region of interest (ROI) of obtainable with our edge device is only 42×16 mm, which is much smaller than the $100 \text{ mm} \times 50 \text{ mm}$ suggested by the IEC 62220-1. Therefore, we can already predict that our results will not allow for observation of the low frequency drop [RSIR05]. However, for a qualitative analysis of the influence of object motion on the MTF, the use of this device should be sufficient.

4.3. Geometry

The geometry for measurement of the MTF is displayed in Fig. 4.1. The same geometry applies when measuring the conversion function. To minimize scatter effects, the source to image-receptor distance (SID) should be a least 1.5 m, and the aperture of the beam at the detector surface should be $160 \text{ mm} \times 160 \text{ mm}$. Any added filtration should be positioned as close to the detector surface as possible. Additional apertures are permissible.

4.4. Measurement of the Conversion Function

In clinical radiography systems, the raw image data can often not be read out by the user. Instead, only the detector response in units of gray level is accessible. The conversion from incident air kerma to displayable gray levels often employs a logarithmic perform, which, when uncorrected, measurably influences the MTF. To analyze and possibly linearize the data, the *characteristic curve* of the detector

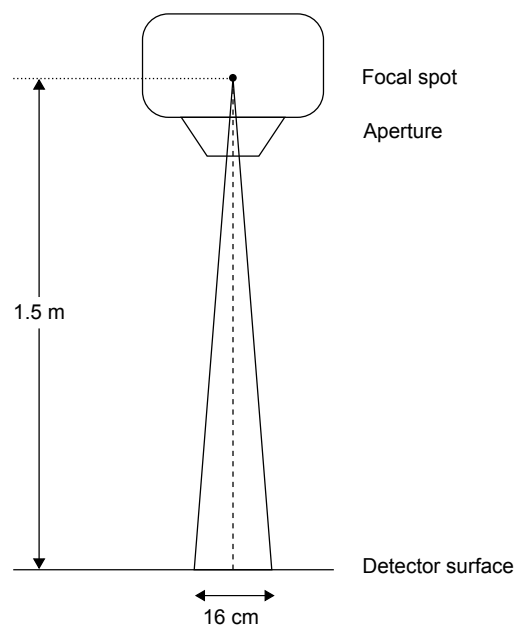


Figure 4.1.: Geometry for the determination of the MTF.

is measured. It contains the detector response in form of the relationship between the incident air kerma input and the gray level output. For determination of the characteristic curve, one measures the incident air kerma and the resulting gray level in the image with homogeneous, full-field exposures over a wide mAs range [NMGK94].

Alternatively, as was suggested by the Siemens development department, the air kerma measurement with a dosimeter can be replaced by extracting the exposure index (EXI) from the meta information of every image. The EXI is calculated as the average air kerma in the central part of the region of interest (ROI). The relationship between air kerma and EXI is therefore strictly linear. To verify this, the exposure was varied over the range 0.5-100 mAs and measured with a dosimeter (DALi type 77217 with ionization chamber type 77334, PTW, Freiburg, Germany) at the detector position. The beam quality was 80 kVp without filtration. The relation between air kerma and EXI is shown in Fig. 4.2. The upper limit of the detector signal is set by the total discharge of the silicon layer and therefore occurs at the same air kerma for all beam qualities, namely the 60 kVp we used for MTF measurement. This saturation is reached at about 200 μGy (EXI \approx 20000). Up to this value, the response is linear. We note, that the EXI value should be kept below 20000 in all images. For MTF measurement it is primarily of interest, if the characteristic curve is linear. In this case, the conversion can be omitted, because the absolute gray levels are of no importance to the final MTF. If the relationship is non-linear, the exact transformation must be calculated and used for data linearization.

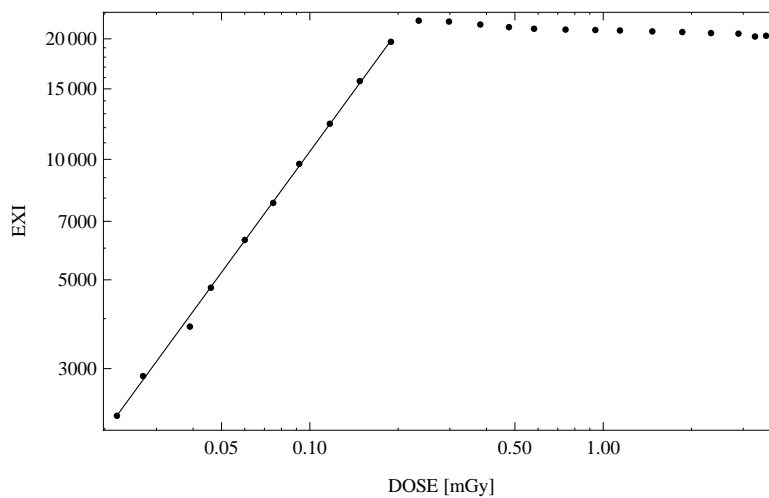


Figure 4.2.: The relation between air kerma and exposure index (EXI) is linear up to the saturation air kerma (\approx 200 μGy).

4.5. Irradiation for determination of the MTF

For measurement of the detector MTF, the edge device is placed on the detector surface. The edge is positioned parallel to the pixel rows or to the pixel columns and then tilted 1.5° to 3° to that axis. This is necessary for the calculation of a subsampled MTF, as will be further explained in 5. For other measurements no instructions exist.

4.6. Corrections of Raw Data

The operations which may be performed with the data before evaluation are specified as the following:

- Replacement for bad pixels with appropriate data
- Homogenization consisting of ...
 - corrections for inhomogeneities of the radiation field
 - corrections for the offset of the individual pixels
 - corrections for the amplification of the individual pixels
- Correction of the geometric distortion and the slope

No further pre-processing is allowed.

4.7. Motion Simulator

MTF measurements using a moving test device are performed with a motion simulator (MotionSim XY/4D, Sun Nuclear Corporation). It was originally designed for quality assurance studies of motion effects in radiation therapy imaging and delivery. The motion simulator offers high precision movement of the test device through programmable motion patterns. The table of the MotionSim XY/4D can be operated along the x-y axes by means of a bipolar stepper motor. It also features movement along the gating surrogate (z) axis, however, this is of no importance for our purposes. The maximum travel distance along the x-y axes is 10.4 cm. The maximum velocity is 5.08 cm/s with a resolution of $0.13\mu\text{m}$ and a bidirectional repeatability of $0.13\mu\text{m}$.

5. Analysis Technique

Over the past decades, several methods for measuring the MTF of imaging systems in a clinical environment have appeared in the literature. They follow one of the two approaches to the MTF which we discovered in 2.1 and 2.2: Either the modulation in the image is measured for one frequency by determining the highest and the lowest brightness in the image of a bar target and simply using Eq. (2.2), or one of the fundamental functions for convolution analysis of the system is used (PSF, LSF or ESF).

The most straightforward method would be the use of a sine wave grating. This was already discussed in 2.1. To acquire enough data points so that the MTF can be interpolated, the modulation needs to be determined at several frequencies. Unfortunately, every frequency requires a separate grating. Because sine wave gratings are difficult to manufacture, they are not a commonly available test device. Instead one makes use of square wave gratings, which are part of the basic quality assurance tests used in every clinic. The modulation determined from a square grating does not equal the modulation obtained with an equivalent sine wave grating, because the rectangular function with frequency ξ not only features the frequency ξ of the sine grating but also higher harmonics. The function that describes the modulation of a square wave grating in dependence of frequency is called the *contrast transfer function* (CTF). A Fourier analysis of the rectangular function leads to the Coltman formula, which relates the CTF to the MTF [Col54].

The use of a square wave grating in combination with the Coltman formula was the standard procedure in the determination of the MTF for analog systems as described by the DIN 6867 [68692]. It does not allow an easy transfer to digital systems. Theoretically, the sampling process can be mathematically undone so that the presampled MTF is determined [Nil01]. However, this involves various numerical steps which result in several FFTs. This way, errors are imposed on the result that are significantly greater than with other methods. The bar target method is therefore no longer an appropriate choice in determining the MTF of digital systems.

In 1992, Fujita et al proposed a method to determine the presampled MTF from the image of a slightly angled slit [FTI⁺92]. The hereby possible construction of a finely sampled LSF was entirely novel and greatly influenced the research during the following years. A thin slit is imaged to obtain the LSF of the system. By angling the slit, instead of averaging over pixel rows, the correct compilation of the data from several pixel rows provides an oversampled LSF, so no information loss occurs at the sampling stage.

Fujita's idea of *oversampling* was later employed by others for edge devices [SFR98], [BGKN03]. It uses the ESF and requires only one computational step more, as the ESF is differentiated to determine the LSF, see Eq. (2.18).

A paper by Samei et al provided a comparison of two edge methods and a slit method in light of a new International Electrotechnical Commission (IEC) standard [62203] for measuring the MTF. One result was that the slit method is much more sensitive to misalignments [SRIC06]. The test edge device which we employed for our measurements (see 4.2) can be seen as a variety on the translucent edge device presented in [SFR98] and [SRIC06].

By now, determination of the MTF by the use of an edge device is an established technique. Several algorithms have been proposed for evaluation of the images. An illustrative comparison can be found in [SBG⁺05]. In the development of our evaluation program, we mainly followed the ideas of Buhr et al in [BGKN03]. This algorithm is also proposed in the IEC standard.

The evaluation program was written in Mathematica. The complete source code is displayed in the appendix A.1. For evaluation purposes, several simulation images were produced. Their source code is shown in A.3.

In the following sections, the analysis technique is discussed in detail. It is illustrated with plots of intermediary results. For these results, a simulation image with a simple blur function (A.3.1) was used as input. Thus, the plots are representative for all evaluated edge images while remaining intelligible.

5.1. Preparation of the image data

In digital radiography, images are created, stored and viewed in the DICOM format (.dcm). DICOM (Digital Imaging and Communications in Medicine) is a standard for transferring images and associated information between various devices in medical imaging. It includes a file format definition as well as a network communications protocol. In addition to the image pixel data, a DICOM file may contain several other attributes which can specify the patient's name, the spatial resolution of the imaging system or the exposure time [Com11a][Com11b].

During exposure, the pixel detectors generate an electric signal which is proportional to the deposited energy and hence also proportional to the incident exposure. To create the image matrix for the DICOM file, the exposure values must be converted into 12-bit grayscale values (0-4095). Our system performs this transformation combined with a normalization. If no additional image processing (windowing, non-linear LUT) is present, the registered range of exposure values is shifted into the range 0-4095 using a linear transformation. However, for this conversion it is also possible to employ a logarithm. In this case, the image data needs to be linearized with the exposure, thus undoing the logarithm transform, prior to any data analysis. The linearization can be achieved by measuring the *characteristic curve* of the system, which relates the pixel value to the incident exposure.

The evaluation program requires as input a data array consisting of pixel values which are linear with exposure. If a simulation image is used, its array can be used directly. If the MTF is to be calculated from an experimentally obtained image, the data array must be extracted from the DICOM file while maintaining the bit depth of 12 bit. We converted the DICOM into a 16 bit PNG by means of the free medical image converter 'dicom2' and cropped to the interesting region featuring the edge transition by means of 'Adobe Photoshop'.

5.2. Determination of the edge angle

Visualize an edge image with a transition from black to white along the horizontal axis. Thus, every line of the image contains some black pixels on the left and some white pixels on the right. In between, one or several pixels mediate the edge transition. If the ESF is build from the data of one single line, the transition is likely to be described by no more than two or three data points. Such insufficient information about the transition can never produce a realistic result for the MTF. However, if the edge was slightly angled with respect to the detector array during exposure, the position of the transition will be slightly different for each line. An adequately small edge angle causes a horizontal shift in the transition of less than one pixel from one line to the next. Combining the information from several lines allows the formation of an ESF that has *subpixel accuracy*. N_{av} describes the average number of lines that induce a horizontal shift of the edge transition of exactly one pixel. To construct the oversampled ESF, N_{int} consecutive lines are used, N_{int} being the nearest integer if N_{av} . N_{int} is called the *oversampling factor*.

The first processing step is to extract the value of N_{int} . If the edge angle α is known accurately enough, N_{av} can be calculated directly by

$$N_{int} = \text{round}(N_{av}) = \text{round}\left(\frac{1}{\tan(\alpha)}\right). \quad (5.1)$$

This relationship is illustrated in Fig. 5.1.

This approach is quite elegant, provided one has access to the edge angle. While clinical environments seldom feature the equipment to measure the edge angle, there exists the possibility to extract the edge angle from the image data. Several approaches with quite different methodologies have been presented in the literature, ranging from simple linear regression [BGKN03] to sophisticated feature extraction techniques [SFR98].

The latter uses a double Hough transform, which was originally designed to recognize the tracks in bubble chamber photographs. Nowadays, the Hough transform cannot only identify lines, but has been extended to other classes of shapes, e.g. circles and ellipses. A formal definition of the Hough transform can be found in [PIK92]. Although it appears elaborate and reliable, the achievable precision in the edge angle determination lies by 0.1° , which is not sufficient for the angle-sensitive calculation of N_{int} and therefore needs to be seconded by an iterative maximization algorithm.

Instead, we will use the algorithm proposed by Buhr et al. [BGKN03]. It subsequently picks

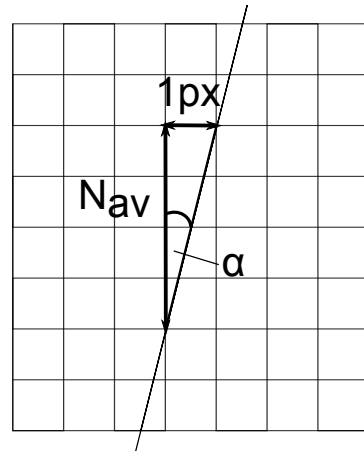


Figure 5.1.: Relationship between the edge angle α and the average oversampling factor N_{av} .

out each line of the image and uses a linear interpolation between the pixel data in each line. The intersection of the interpolating function with the 50 %-level determines the edge location with subpixel accuracy. The position of the edge shifts from line to line, so that a linear regression can be used to fit a straight line through the edge estimates. The average number of consecutive lines that produce a lateral shift of 1 px can be calculated from the average slope b by

$$N_{av} = \frac{1}{b}. \quad (5.2)$$

N_{av} is then rounded to the nearest integer N_{int} . We can also calculate the edge angle α from b via

$$\alpha = \arctan(b). \quad (5.3)$$

For a thorough understanding of this method, the code snippet in Part 1 of A.1 for the generation of the list containing the edge estimates can be isolated and the positions of the data points observed from line to line. In Fig. 5.2a we exemplarily see the ESF data from one line with linear interpolation. The positions of the data point shift from line to line along the transition. The acquired edge estimates of all lines are displayed in Fig. 5.2b. From this list, the average slope b is determined. We notice the oscillation in the edge position. Depending on the position of the data points along the edge transition in one line, the interpolated straight lines slightly change their slopes and the intersection with the 50 %-level varies. This oscillation is periodic with the vertical shift of the edge of 1 px and therefore with N_{av} .

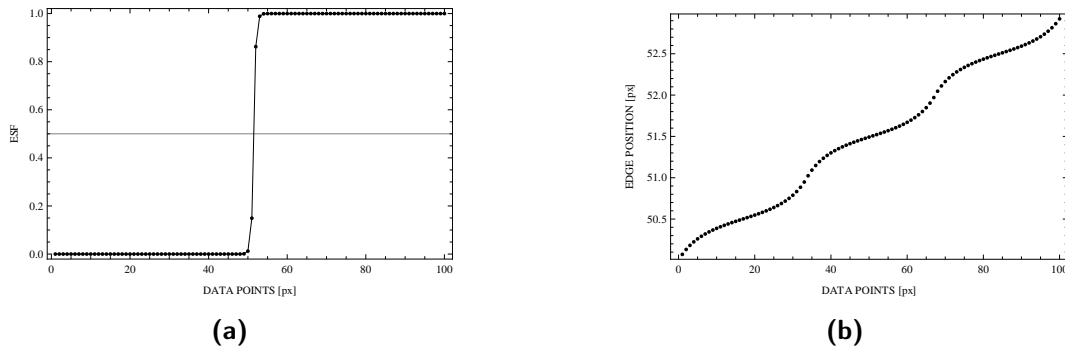


Figure 5.2.: Illustration of the edge angle determination. (a) ESF of a single line with linear interpolation between the data points, (b) Position of the edge transition (intersection with 50 %-level) in each line.

In 6.1 we will discuss the precision of this method for determining the edge angle, including the influence of the oscillatory behavior.

The IEC 62220-1 [62203] specifies an angle range of $1.5^\circ - 3^\circ$ in experimental images for MTF calculation, corresponding to values of $N_{int} = 38 - 19$.

5.3. Construction of the oversampled ESF

After N_{int} has been determined, the oversampled ESF can be constructed from the data of N_{int} consecutive lines. As already mentioned, this was first proposed in 1992 by Fujita et al [FTI⁺92]. In the simplified example in Fig. 5.3 with $N_{\text{int}} = 4$, the lines are interlaced in the following way: We start with pixel 1 of line 1, followed by pixel 1 of line 2, and so on until pixel 1 of line N_{int} . This is followed by pixel 2 of line 1, the procedure continues for all second pixels, and so on until the last pixel of line N . If the orientation of the edge angle changes, the sampling direction must be reversed. The pixel spacing s of the subsampling grid is the original pixel spacing p divided by the oversampling factor $s = \frac{p}{N_{\text{int}}}$.

Note that through the introduction of a subsampling grid, the Nyquist frequency has increased from $\xi_{\text{Ny}} = 1/p$ to $\xi_{\text{Ny}} = 1/s$.

The process of interlacing itself is not complicated, however, the resultant oversampled ESF is generally quite noisy. In such cases, it is highly commendable to reduce the noise level in the ESF in some way before proceeding with the next steps. In 6.2, we will discuss several techniques in detail, such as smoothing and averaging of multiple representations of the ESF.

By interlacing the image data in the way described above, we introduce a systematic error into the calculation: The subsampling grid is assumed to be regular, while the true subsampling grid will generally not feature equidistant subsampling distances. The assumption of a regular subsampling induces phase errors, which show up as kinks in the oversampled ESF, see Figs. 5.4a and 5.4b. The deviations are stronger if N_{av} is centered between to integers, and less so if N_{av} lies close to the nearest integer. The kinks appear periodic with the original sampling distance p . In 6.1 we discuss the influence of phase errors on the MTF.

1	5	9	13	17
2	6	10	14	18
3	7	11	15	19
4	8	12	16	20

Figure 5.3.: Sampling direction in the case of $N_{\text{int}} = 4$.

5.4. Derivation of the oversampled LSF

To calculate the oversampled LSF, the ESF needs to be differentiated. As we deal with discrete data, it is not possible to perform the differentiation via calculating the analytical limit of a difference quotient. One way of overcoming this difficulty is to use a model that is fitted to the experimental data of the the edge response. In doing so, one might deprive oneself of interesting discoveries, because a fixed form of the data is assumed to early along the way. Instead, all state-of-the-art algorithms employ finite element differentiation. Depending on the required accuracy, one can implement a naive onesided differentiation, a symmetric central

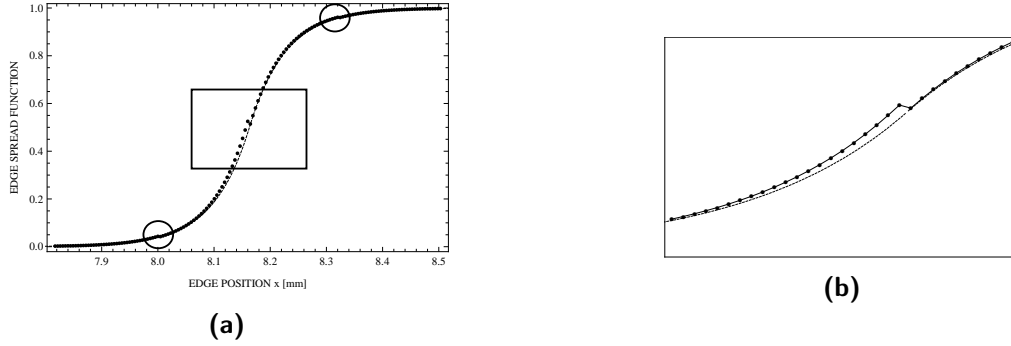


Figure 5.4.: Phase error in the oversampled ESF induced by rounding N_{av} to the nearest integer N_{int} . The true ESF is shown for comparison. (Example: $N_{av} = 33.5$) (a) Periodic kinks in the ESF, (b) Zoom showing one of the kinks.

difference (both with two reference points for one evaluation point) or formulas which include terms of higher order.

The naive one-sided approach to numerically differentiate a function $f(x)$ is

$$f'(x) \approx \frac{f(x+h) - f(x)}{h}, \quad (5.4)$$

where h is the sampling distance. The truncation error that is induced by this approximation can be calculated by a Taylor expansion. It is in the order of the sampling distance h .

A more stable version can be created by placing the reference points symmetrically around the evaluation point:

$$f'(x) \approx \frac{f(x+h) - f(x-h)}{2h}. \quad (5.5)$$

The truncation error scales with the square of the sampling distance h^2 .

It is also possible to draw on four or more reference points for calculating the differentiated function for one evaluation point. The symmetric 4-point formula

$$f'(x) \approx \frac{f(x-2h) - 8f(x-h) + 8f(x+h) - f(x+2h)}{12h} \quad (5.6)$$

has a truncation error of the order of h^4 , however, this trend does not continue further: Expressions with higher terms are more prone to cancellation, if h gets too small.

In practice, the symmetric central difference (5.5) is the most commonly used formula. It provides an adequate and stable differentiation method for the oversampled ESF. It is possible to implement Eq. (5.5) straightforward for all elements in the ESF list. Alternatively, the ESF can be convolved with a $[0.5, 0, -0.5]$ kernel.

The finite element differentiation is not without problems either. The approximation of the true derivative of the ESF is based on the slope between neighbouring pixels. If the system is not sufficiently oversampled, this discretization induces an error [CF87]. This error can be corrected for in the frequency domain. For further details, see 5.6.

As a result, we have now obtained a list which contains the data of the oversampled LSF.

5.5. Fourier transform to obtain presampled MTF

In order to finally determine the presampled MTF, the oversampled LSF must be Fourier transformed. The Fourier transform provides a bridge between two different representations of the same function. We will indicate quantities in the time domain by lowercase letters, $h(t)$, and the associated representation in the frequency domain by capital letters, $H(f)$. The continuous Fourier transform equations are

$$H(f) = \int_{-\infty}^{\infty} h(t)e^{2\pi ift} dt \quad (5.7)$$

$$h(t) = \int_{-\infty}^{\infty} H(f)e^{-2\pi ift} df. \quad (5.8)$$

There exist other conventions which employ ω instead of f , whereby factors of 2π arise. The above convention needs fewer factors of 2π , which is also helpful when we move on to the transform of discretely sampled data.

If the function $h(t)$ is sampled with M sampled values and the sampling interval Δ ($h(t) \hat{=} h(k\Delta)$, with $k = 0, 1, 2, \dots, M-1$), its discrete Fourier transform can be approximated as

$$H(f_n) = \int_{-\infty}^{\infty} h(t)e^{2\pi if_n t} dt \approx \Delta \sum_{k=0}^{M-1} h_k e^{2\pi i k n / M}. \quad (5.9)$$

The discrete frequency values are

$$f_n \hat{=} \frac{n}{M\Delta}, \quad n = -\frac{M}{2}, \dots, \frac{M}{2}, \quad (5.10)$$

which is exactly the Nyquist frequency range.

When implementing the Fourier transform, it is highly recommended that the input consists of M sampled values with M an integer power of 2 [PTVF07]. Computational systems nowadays almost all use a Fast Fourier Transform. This algorithm splits a discrete Fourier transform of length M into two discrete Fourier transforms of length $M/2$. This is used recursively until the data is subdivided to Fourier transforms of length one. In setting M to an integer power of 2, much trouble can be avoided. If the data does not have the appropriate length, it can be padded up with zeros to the next power of 2.

After the discrete Fourier transform, we have gained the 1-dimensional MTF. According to its definition, the MTF must be unity at zero frequency. We therefore normalize the MTF to its value at zero frequency. Apart from some small corrections for angling the edge and differentiating the ESF, this is the final result. The MTF is only valid up until the Nyquist frequency. However, in 6.3 we will see that the oversampling increases the Nyquist frequency to such a degree that aliasing effects can be neglected.

5.6. Corrections

Correction for finite-element differentiation The MTF needs to be corrected for the differentiation process described in 5.4. In finite-element differentiation, the information of neighboring pixels is used to estimate the differential quotient. Such linear interpolation between data points does not produce the same result as differentiation of the LSF from an analytical ESF and subsequent sampling. Following an approach by Cunningham et al [CF87], we calculate the frequency response of the finite-element differentiation and compare it to the frequency response of analytical differentiation.

In 5.4, the LSF was obtained via the central difference

$$\text{LSF}(x_j) = \frac{1}{2s} (\text{ESF}(x_{j+1}) - \text{ESF}(x_{j-1})). \quad (5.11)$$

This can be expressed as the convolution of the ESF with the finite-difference operator Δ

$$\text{LSF}(x) = \text{ESF}(x) * \Delta \quad (5.12)$$

$$\Delta = \frac{1}{2s} (\delta(x+s) - \delta(x-s)). \quad (5.13)$$

The Fourier transform of Δ gives us the frequency response of the finite-element differentiation

$$\mathcal{F}(\Delta) = \text{OTF}_{\text{est}}(\xi) = 2i\xi_{Ny} \sin\left(\frac{\pi\xi}{\xi_{Ny}}\right) \quad (5.14)$$

with $\xi_{Ny} = 1/2s$.

In analytical differentiation, the ESF is convoluted with the derivative of the impulse function

$$\text{LSF}(x) = \frac{d\text{ESF}}{dx} = \text{ESF} * \delta'(x). \quad (5.15)$$

Fourier transform of $\delta'(x)$ provides us with the result

$$\mathcal{F}(\delta'(x)) = \text{OTF}_{\text{true}}(\xi) = 2\pi i \xi. \quad (5.16)$$

The ratio of the estimated MTF to the true MTF is the MTF of the derivation filter

$$\text{MTF}_{\text{deriv}} = \frac{\text{MTF}_{\text{est}}}{\text{MTF}_{\text{true}}} = \text{sinc}\left(\frac{\pi\xi}{\xi_{Ny}}\right). \quad (5.17)$$

The data of the discrete MTF is divided by the correspondent value of $\text{MTF}_{\text{deriv}}$.

Correction for the distance between edge and subsampling grid points The usage of the image data as a discrete ESF suggested that the sampling grid points lie in the direction perpendicular to the edge. In truth, the x axis on which the grid points are located is not in the direction perpendicular to the edge, due to the edge angle. The distance between the edge and the sampling grid points is smaller by a factor of $\cos(\alpha)$. This can be compensated for in the frequency domain by scaling the spatial frequency ξ with the factor $1/\cos(\alpha)$.

6. Results from Simulation

Our first task must be to verify the behavior of the evaluation program. For this, we need images that feature an edge transition whose analytical description is known. The MTF can then be calculated analytically and the discrete MTF results compared with the analytical solution. The edge transition should be variable, so that systems with different resolution can be imaged. It should also be possible to add noise. The edge angle must be variable to verify the calculation of the edge angle from the image data. It could be interesting to separate the sampling step to verify whether the MTF is actually presampled.

The standard edge transition which we chose for our simulations is a sigmoid curve

$$ESF_{sim}(x) = \begin{cases} 1 - \frac{1}{2} \cdot e^{-rx} & x \geq 0 \\ \frac{1}{2} \cdot e^{+rx} & x < 0. \end{cases} \quad (6.1)$$

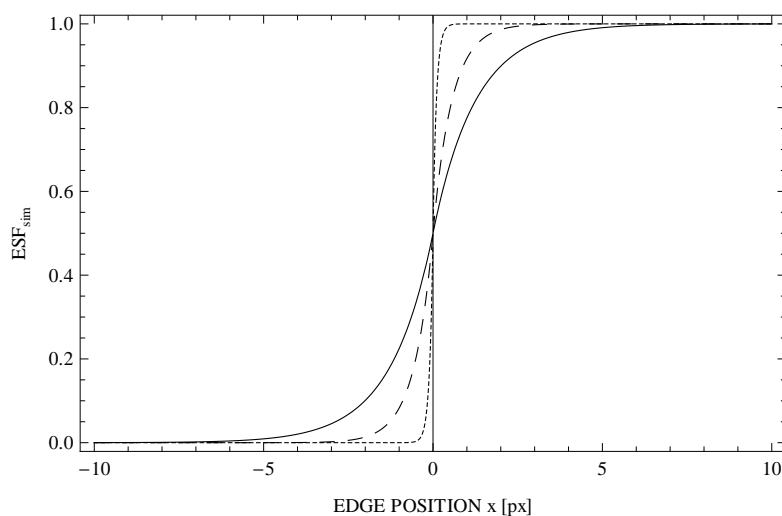


Figure 6.1.: Edge transition for three different values of parameter r . **Continuous line:** $r=0.8$, **dashed line:** $r=1.8$, **dotted line:** $r=10$.

The value of r determines the slope of the edge transition. Fig. 6.1 illustrates the transition for three different values of r . The central curve with $r=1.8$ has approximately the shape that is found with out radiographic imaging system by SIEMENS. Differentiating this function gives us the LSF as

$$\text{LSF}_{\text{sim}}(x) = \begin{cases} \frac{1}{2} \cdot r \cdot e^{-rx} & x \geq 0 \\ \frac{1}{2} \cdot r \cdot e^{+rx} & x < 0. \end{cases} \quad (6.2)$$

The Fourier transform of the LSF provides us with the Lorentzian shaped MTF

$$\text{MTF}_{\text{sim}}(\xi) = \frac{r^2}{r^2 + (2\pi\xi)^2}. \quad (6.3)$$

To produce a simulation image, an array of arbitrary size is allocated. In each line, the entries are filled with values of the function $\text{ESF}_{\text{sim}}(x)$, x is interpreted in px. From column to column, $\text{ESF}_{\text{sim}}(x)$ is shifted along the x -axis by $\tan(\beta)$. This produces the image of an edge with the edge angle β . Details can be looked up in the Mathematica documentation A.3.1.

This standard image can be modified to add noise or include effects of the sampling aperture.

To allow comparison with experimental images when evaluating the MTF, the pixel spacing (which is not defined in the image itself) was assumed to be 0.16 mm in both directions. The pixel spacing is a necessary value, because the MTF can otherwise not be displayed in 1/mm, but only in 1/px.

6.1. Analysis of Phase Errors

In this first test of the algorithm, we pay special attention to the accuracy of the angle determination, on the one hand because the determination of N_{av} depends very sensitively on the angle, on the other because we are forced to induce an error by rounding N_{av} to N_{int} which cannot be undone. All subsequent steps in the algorithm produce either exact results within the machine accuracy or induce errors which can later be compensated (e.g. finite-element differentiation). We successively analyze the two critical steps in the algorithm.

Using the transition function ESF_{sim} in (6.1), simulation images were generated for three values of r (0.8, 1.8 and 2.5) and the edge angle varying from 1.5° to 3.0° in steps of 0.1° . This covers the whole range of approved angles for MTF analysis and focuses on images with r in the region around $r = 1.8$, which we expect to resemble the experimental images. To judge the accuracy of the determination of the edge angle α , we observe the absolute error in the angle for all three values of r in Fig. 6.2.

Details on the determination of the edge angle can be found in 5.2. The process is less error-prone for lower r , because then the slope of the transition is smaller and the regression line can be determined more accurately. We further notice that $\Delta\alpha$ is oscillating. This is a copy of the oscillating behavior of the position of the edge transition, that we became acquainted with in 5.2. The oscillation grows stronger for greater values of r , because there are fewer data points in the edge transition due to the greater slope of the transition function. It is less problematic for greater angles, for which N_{av} is smaller. In 5.2 we learned that the oscillation of the edge position is periodical with N_{av} . If N_{av} is smaller, the oscillation can

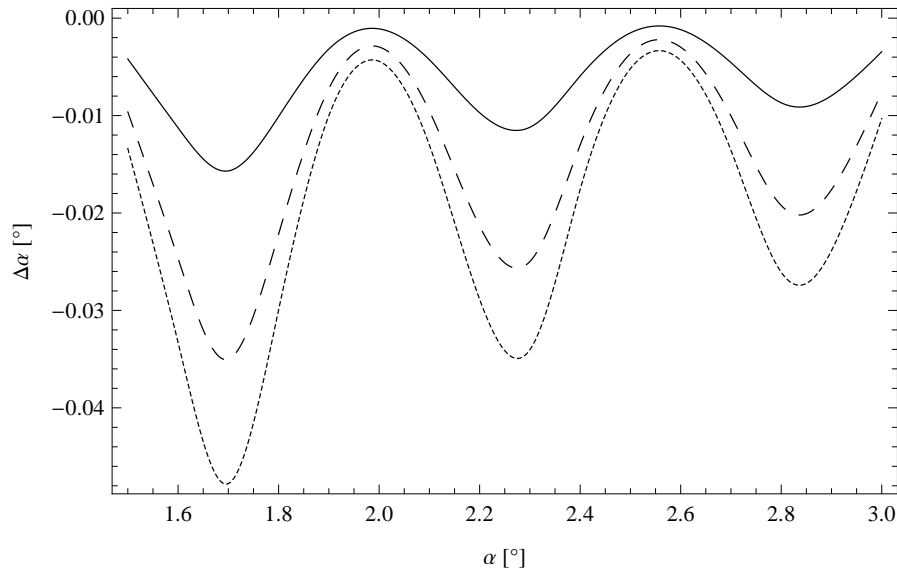
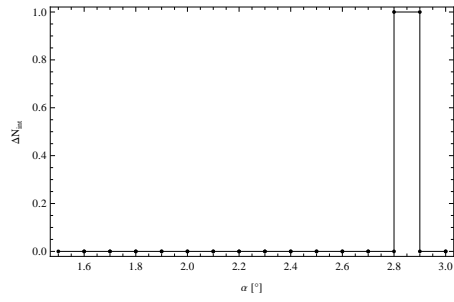
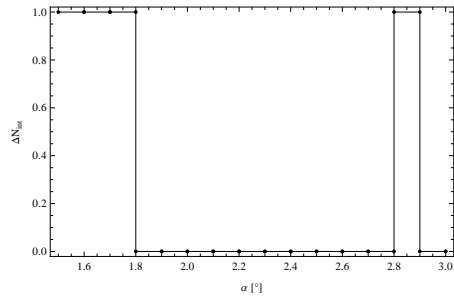


Figure 6.2.: Absolute error in the edge angle α for three values of r . Interpolation order: 3. Continuous line: $r = 0.8$, dashed line: $r = 1.8$, dotted line: $r = 2.5$.

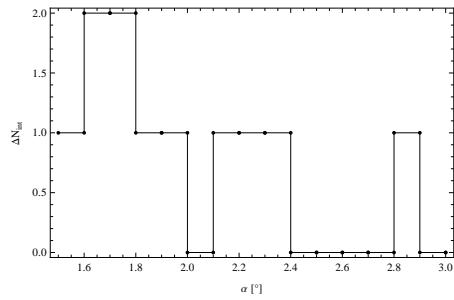
be averaged over a greater number of periods, which increases the accuracy of the regression. It is also helpful to utilize the full possible height of the image, which will also increase the number of periods that are used for averaging. Note that while the MTF construction itself only needs N_{int} consecutive rows of the image, as much rows as possible should be used for the accurate determination of the edge angle.



(a) $r = 1.8$



(b) $r = 2.5$



(c) $r = 10$

Figure 6.3.: Systematic error of N_{int} induced by both erroneous angle determination and rounding for three values of r . (a) Error due to rounding of N_{av} . (b),(c) Errors from linear regression increase with higher r .

The second error is the rounding of N_{av} to the nearest integer N_{int} . This is necessary for the formation of the ESF, which must have an integer length. In Figs. 6.3a, 6.3b and 6.3c we see the influence of the composition of both errors on N_{int} . Most peculiar is the deviation around 2.8° for all values of r . In contrast to the error from the linear regression, the error through rounding increases with the angle. As N_{av} gets smaller, the relative error in rounding to the nearest integer gets larger. This error is dominant for $r \lesssim 2.1$; for greater values of r , the error from linear regression takes effect. For further illustration of this effect, Fig.6.3c shows the offset in N_{int} for $r = 10$. As α is always below value, ΔN_{int} is always positive.

We have learned something about the potential pitfalls in the first part of the algorithm. When calculating the MTF from experimental data, a comparison between the obtained MTF and MTFs from simulation images is recommended. This way, the corresponding value of r can be estimated and (together with the edge angle) used as a basis for predicting deviations in N_{int} . If the MTF is calculated with a smaller value of N_{int} , one still needs to verify which is closer to the 'true' MTF. This can be achieved using a maximization algorithm [SFR98]. It calculates the best N_{int} estimate by integrating the MTF within a certain frequency range and determining the MTF which produces the highest value.

We will now briefly demonstrate the impact of N_{int} on the MTF. Note that for comparison reasons the pixel spacing was assumed as $p = 0.16$ mm, the same as for the experimental images. In Fig. 6.4a we see the calculated MTF along with the analytical solution for $r = 2.5$ and $\alpha = 1.9^\circ$. The absolute error for this angle is small (see Fig. 6.2) and the corresponding value of $N_{av} = 30.14$ is close to the next integer $N_{int} = 30$. Consequently, the resulting MTF data points coincide very well with the analytical MTF. In contrast to this optimum, we observe in Fig. 6.4b the MTF of a simulation image with $r = 2.5$ and $\alpha = 1.7^\circ$. We know from the above considerations, that in this

case N_{int} is overestimated by $\Delta N_{int} = +1$. Starting at about 2 1/mm , the discrete MTF data points are below the true value, increasingly so with higher spatial frequency. If N_{int} is manually adjusted, the deviation does not begin until a spatial frequency of about 3.5 1/mm (which is greater than the Nyquist frequency of the system) and is generally less dominant. We notice however, that the deviation is not completely nullified. The reason is, that for $\alpha = 1.7^\circ$ the value of N_{av} does not lie close to the nearest integer but is rather centered between two integers ($N_{av} = 33.69$). In these cases, the discrepancy between the true subsampling grid with nonuniform subsampling distances and the assumed regular subsampling grid induces phase errors, which we already encountered in 5.3. Buhr et al. have proposed a method which averages multiple representations of the ESF to reduce the systematic phase errors [BGKN03]. Two groups of N_{int} consecutive lines which overlap by $N_{int}/2$ will produce systematic errors of equal magnitude but opposite sign. Averaging this groups should reduce the error. This averaging algorithm is incompatible with averaging algorithms for noise reduction which we will discuss in 6.2 and which use non-overlapping representations of the ESF. Since the methods for noise reduction are very effective and commendable for most purposes, we will not further concern ourselves with the reduction of phase errors.

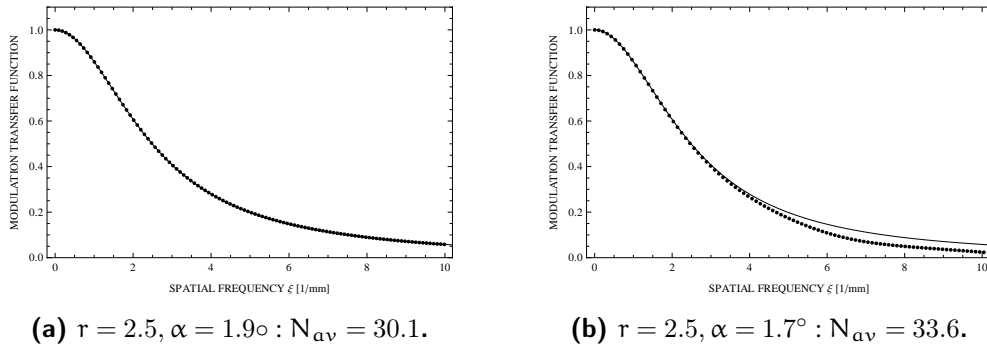


Figure 6.4.: Effect of phase errors on the MTF

If not mentioned otherwise, all following simulations are performed with an edge angle of $\alpha = 1.9^\circ$, which results in an oversampling factor of $N_{int} = 30$ close to the actual value $N_{av} \approx 30.1$.

6.2. Reducing noise in the MTF

Noise is an indication of a random process. In x-ray imaging, there are three important random phenomena:

The number of photons that leave the x-ray source follow a Poisson distribution. The number of photons that pass unaffected through the object is Binomial distributed. The number of photons that are captured by the detector is also Binomial distributed. If a Poisson random process is followed by a Binomial random process, the Binomial selection 'thins' the Poisson distribution. It can be shown that the result is still a Poisson distribution, but with reduced mean [Mac83]. In our case, a Poisson random process is followed by two Binomial selections. So the overall noise distribution in x-ray imaging is approximately Poisson.

The above mentioned distributions are mathematical descriptions of random variables (here: number of photons), so-called probability distribution functions. They give the probability that the random variable X will take on a value less than or equal to a value k . The Poisson distribution function

$$\Pr[X = k] = \frac{\alpha^k}{k!} \cdot e^{-\alpha} \quad (6.4)$$

with parameter $\alpha > 0$ has the mean $\mu_k = \alpha$ and the variance $\sigma_k^2 = \alpha$. It is characteristic for events which occur independently and with constant rate during a fixed of time and/or space.

To quantify noise, it is reasonable to compare the noise level with the system level. For this, we employ the *signal-to-noise ratio* (SNR). It can be defined as

$$\text{SNR} = \frac{I_s - I_b}{\sigma_b}, \quad (6.5)$$

where I_s and I_b are the signal and background intensities, respectively, and σ_b is the standard deviation of the background intensity [PL06]. The SNR is reduced either by an increase in noise level, or by an increase in blur in the image (as this decreases the contrast). A higher SNR indicates that the signal is a more accurate representation of the investigated process, while a lower SNR indicates a less accurate representation [PL06]. The SNR is a useful tool for comparing images taken with varying imaging parameters or from different imaging modalities.

In finding suitable simulation images which have approximately the same noise properties as the experimentally obtained images, we started off with the already familiar noiseless image and added Poisson noise of appropriate mean so as that the SNR is comparable to that in experimental images ($\text{SNR} \approx 180$). The noise can be only positive or only negative off-set or arbitrarily mixed. The noise level can be independently adjusted for positive and negative off-sets. For further details see the Mathematica code (A.3.2). The response function is given by Eq. (6.1), the parameters used in this section are $r = 1.8$ and $\beta = 1.9^\circ$. We found the choice of r and β did not influence the results.

We will now examine two methods which aim at reducing the noise level in the image data.

6.2.1. Smoothing

A publication by Boone proposes to smooth the LSF to reduce the noise in the data [Boo01]. We will describe the basic aspects of smoothing and test different smoothing algorithms for simulated images.

In smoothing, the essential features and the form of a signal are extracted and preserved, while noise or other rapid, random changes in amplitude are reduced. This is achieved by comparing the value of each data point to the values of its adjacent points. Grave deviations in any direction are replaced by values which fit more neatly into the ensemble.

Most smoothing algorithms replace the value of a single data point by the weighted average of its surrounding points. The number of adjacent points which partake in the calculation and the set of coefficients determine the outcome of the smoothing.

The simplest smoothing algorithm is the *rectangular smoothing*, in which the w used adjacent points all have equal weight. A rectangular smoothing of width 3 transforms the initial data point I_j into a smoothed data point S_j in the following way:

$$S_j = \frac{I_{j-1} + I_j + I_{j+1}}{3}. \quad (6.6)$$

The composition of two rectangular smooths gives a *triangular smooth*. The coefficients increase in steps of one like a pyramid towards the middle. For example for a 5 pt-width:

$$S_j = \frac{I_{j-2} + 2I_{j-1} + 3I_j + 2I_{j+1} + I_{j+2}}{9}. \quad (6.7)$$

There are other algorithms which use techniques different from the sliding-average technique explained here. For example, the Savitzky-Golay smooth uses least-square fittings of polynomials to segments of data [SG64].

If applied carelessly, smoothing can result in significant alterations of the signal [O'H91]. Fig.s 6.5 demonstrates the effects of a rectangular smoothing algorithm with different smooth widths on a Gaussian-shaped peak to which Poisson noise was added. The half-width of the peak contains 35 data points. The two superimposed lines are the results of a rectangular smoothing of width 9 pt (dashed) and 55 pt (dotted). The noise is progressively reduced with smooth width, but the absolute peak height is reduced and the bandwidth increased, which strongly alters the line shape. As a rule of thumb for peak-type signals, one can calculate the *smooth ratio*, which is the ratio of the smooth width w and the number of points N in the half-width of the peak. For assuring that peak height and width are not significantly altered, a smooth ratio below 0.3 is suggested [O'H91]. In our example, the smooth ratios would be 0.29 and 1.6, respectively.

The smooth width is typically an odd integer, as the coefficients are then symmetrically distributed around the central point. This ensures that signal peaks and other striking features remain fixed in their positions along the x-axis. If the signal is very noisy, it is recommended to use successive smooths with smaller width rather than a single smooth with great width. This is generally more effective. The effect of n smooths of width w equals a single smooth of width $nw - n + 1$ [O'H91].

Boone proposes to smooth the noisy LSF with a triangular smoothing (3 px wide for a subsampling factor $N=10$) [Boo01]. As an exact shape is essential for calculating the MTF, the algorithm must not alter the curve shape in such a way that it influences the MTF. We will now test potential smoothing algorithms on ESF data of a simulated edge image with analytically known edge response. (Boone used a slit method. Therefore, he directly acquired a presampled LSF with no need of differentiation. We will smooth the presampled ESF instead, as this is our initial data set.)

The edge image was created as described in section 6 with an image size of 100 px \times 100 px. The number of data points in the half-width of the LSF-peak was $N = 12$, which is approximately the number of points to be expected in the images derived from experiment.

The tested algorithms were triangular smooths of 3 px width (Algorithm 1), 9 px width (Algorithm 2) and 25 px width (Algorithm 3). In Fig. 6.6, we observe the ESF, LSF and MTF for the three smoothed data sets in comparison to the unsmoothed data. The parameters for the added noise were chosen in such a way that the ESF, LSF and MTF possessed noise levels comparable to those found in experimentally obtained images. The apparent quantization in the unsmoothed LSF results from the calculation of the Poisson noise (see A.3.2) and could not be circumvented for the desired noise level. While a little irritating for the eye, they allow an estimation of the initial noise level.

Algorithm 1 (Figs. 6.6d,6.6e,6.6f) represents a conservative smoothing with a width that is acceptable with regard to the smooth ratio. The noise in the ESF and LSF is visibly reduced, but the MTF looks much the same as before.

The smooth ratio for Algorithm 2 (Figs. 6.6g,6.6h,6.6i) is already above the recommended value of 0.3. ESF and LSF are much clearer represented and there are at least no eye-catching deviations in the MTF. However, the noise level in the MTF is not nearly as improved as one might have hoped for, so this algorithm can be ruled out as well.

The smooth width of Algorithm 3 (Figs. 6.6j,6.6k,6.6l) is by far greater than recommended for this data set. We listed it because the noise is reduced as desired. However, the great

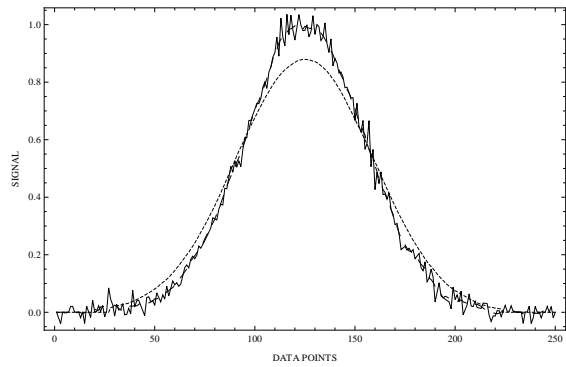


Figure 6.5.: Rectangular smoothing of a Gaussian-shaped peak with smooth widths 9 pt (dashed) and 55 pt (dotted). There are 35 data points in the half-width of the peak.

width destroys the shape of the MTF. The data deviates so much from the actual values that the information content is actually null.

From these results we can derive the conclusion that the improvements in ESF and LSF do not justify the use of a triangular smoothing algorithm, because the MTF noise level is for the most part unaffected. It is possible to explain these results following the theory of transfer functions laid down in Chapter 2. While ESF and LSF are functions in the position space, the MTF is function in the frequency space. Convolution of functions in the spatial domain equals multiplication of the Fourier transformed functions in the frequency domain. For example, the Fourier transform of a rectangular smooth of width w would be a sinc function with the first zero at $1/w$. The Fourier transform of a 3 px-width rectangular function for our system with pixel size 0.16 mm and subsampling factor $N_{int}=30$ would result in a sinc function with the first zero at a frequency of 187.5 1/mm. We are only interested in frequencies up to 10 1/mm, so multiplying our MTF with this function has no use whatsoever. Even worse, this is not only not effective, it is no smoothing of the MTF at all. In multiplication, the MTF values are merely reduced in accordance to the value of the sinc function, with ever more reduction for higher spatial frequencies. This plausibly explains the gradual decrease in the MTF for great smooth widths (Fig. 6.6l).

Smoothing the ESF or LSF can be discarded. The data should be processed unsmoothed. If the MTF is to be determined at a frequency ξ for which no data point exists, it can be estimated by the surrounding points, which can be seen as a local smoothing. [iD13] suggests to use the data points in the interval $\xi - 0.5\xi_{int} \leq \xi \leq \xi + 0.5\xi_{int}$ with $\xi_{int} = 10^{-2} \cdot \text{pixel spacing}^{-1}$.

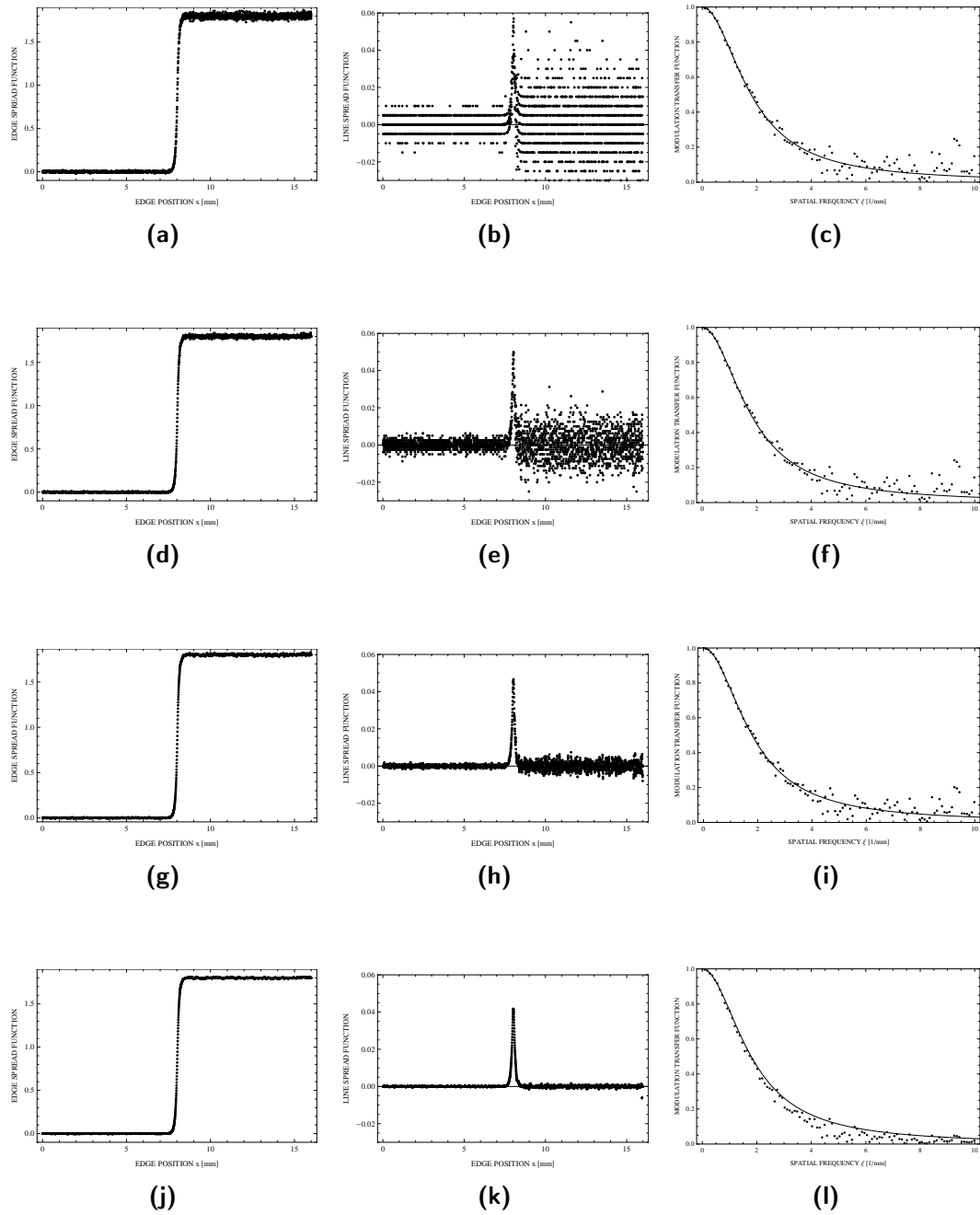


Figure 6.6.: Effects of different smoothing kernels on noisy data. Left side: ESF, Middle: LSF, Right side: MTF.

(a),(b),(c): Original data. (d),(e),(f): Conservative smoothing. (g),(h),(i): Smooth ratio slightly higher than recommended. (j),(k),(l): Extremely high smooth ratio.

6.2.2. Averaging using several layers of data

Alternatively to smoothing, Buhr et al. suggested to employ several representations of the ESF from independent data sets [BGKN03]. Either several MTFs could be calculated and averaged, or the ESF of several oversampled ESFs can be calculated from which the MTF is determined. Fisher writes in [Fis82] that uncorrelated noise in the image does not only result in a noisy MTF but also a positive bias error, because the MTF has only absolute values, which cannot be negative. We will therefore test only the effects of averaging the ESFs.

The main idea is to create several ESFs from non-overlapping data sets and combine them to one average ESF which is used for MTF analysis. In every data set of N_{int} consecutive lines, the edge transition will occur at a different subpixel, so the data sets cannot be merged without shifting so as that the edge transitions are in the same subpixel. Buhr accomplishes this by selecting all data points within the 30 % and 70 % level around each edge transition, calculating a regression line and identifying its intersection with the 50 % level and round this to the nearest subpixel. This way, the edge transitions can be matched with subpixel accuracy. Instead of this slightly laborious approach, we make use of the exact position of each data set in the image data. The original algorithm chooses a set of N_{int} lines from the middle of the image, starting at `start` (see A.1.3). The other ESF data sets are generated by shifting `start` N_{int} lines in one or the other direction. This implies that the edge position has also moved N_{int} subpixels, so the ESFs can be shifted appropriately and be averaged without localizing the edge position. Both methods suffer from the same drawback: The number of subpixels in the averaged ESF is reduced compared to the original width of N_{int} times the image width, increasing with the number of data sets used for averaging. This is inevitable, because shifting the ESFs so that the edge transitions take place at the same subpixel goes along with clipping the sides. The length reduction is minimized when the data sets are directly adjacent. For m adjacent, non-overlapping data sets of N_{int} lines, the length reduction is $(m - 1) \cdot N_{int}$. Therefore, this method is not commendable images with relatively small width. Clipping the sides might prevent the investigator from discovering the low-frequency drop in the LSF.

The edge image was created as in the section before, this time for an image size of 210 px x 210 px. For $N_{int} = 30$, this allows up to 7 data sets for the averaging process.

Fig. 6.7a shows the original noisy MTF data. Figs. 6.7b, 6.7c and 6.7d illustrate the reduction of noise if 3, 5 or 7 data sets are used for averaging the underlying ESF. We observe a continuous improvement over the whole frequency range if more data sets are employed. No distortions or amplitude losses are present.

We conclude that calculating an average ESF to reduce noise in MTF analysis can be recommended, provided the image width permits the reduction.

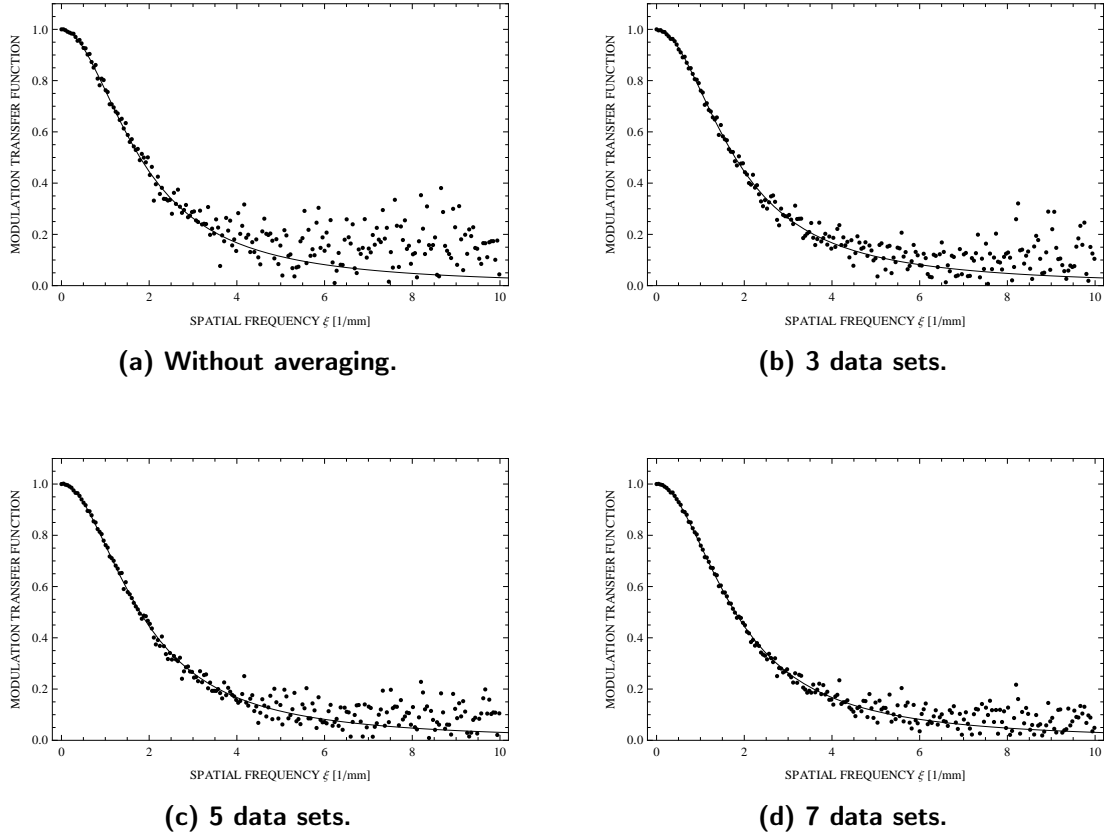


Figure 6.7.: Averaging of multiple ESF representations effectively reduces the noise level without altering the MTF curve shape.

6.3. Sampling and Aliasing

The presampled MTF consists of the analog input and the influence of the sampling aperture, i.e. the pixel dimensions. In 2.3.3 we already derived that the influence of the sampling aperture is in the same order as the influence of the geometric unsharpness. The impulse response of the sampling aperture is a rectangular function of the pixel dimensions a and b :

$$\text{PSF}_S(x, y) = \Pi\left(\frac{x}{a}\right) \cdot \Pi\left(\frac{y}{b}\right). \quad (6.8)$$

The MTF component is a sinc function, with the first zero along the x -axis at $1/a$ and the first zero along the y -axis at $1/b$:

$$\text{MTF}_S(\xi, \eta) = \text{sinc}(\pi a \xi) \cdot \text{sinc}(\pi b \eta). \quad (6.9)$$

The simulation images were created by modification of the standard image. For details, see A.3.3. ESF_{sim} (6.1) was convoluted with a rectangular function of one pixel width. For the standard image, the value of one pixel is determined by the value of ESF_{sim} in the center

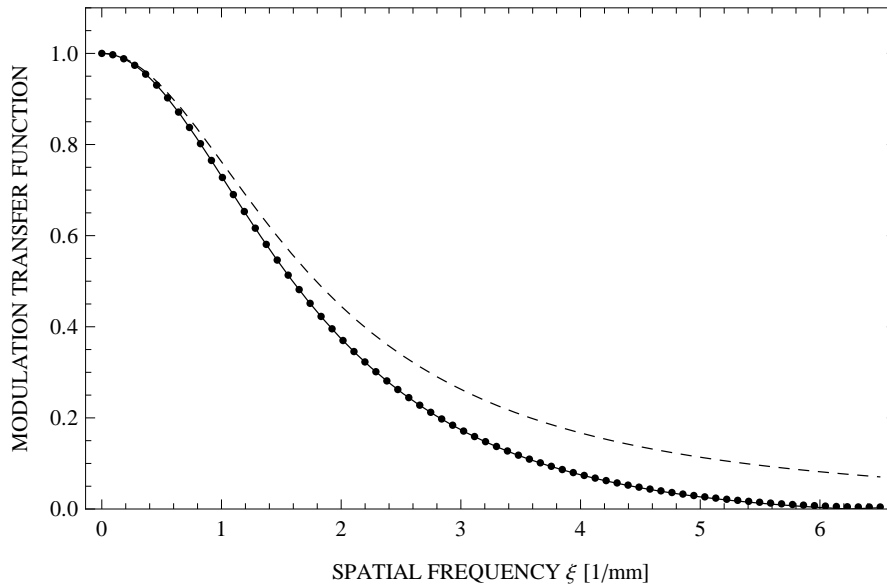


Figure 6.8.: Resolution loss introduced by the sampling aperture. **Continuous line:** Analytical MTF of standard image without sampling, $r = 1.8$. **Data points:** Calculated MTF of standard image $r = 1.8$ with pixel spacing $p = 0.16$ mm. The first zero in the sampling MTF is visible at $1/p = 6.25$ Lp/mm.

of the pixel. Here, the value is calculated by averaging the ESF_{sim} values over the width of one pixel. This reduces the resolution, as can be seen in Fig. 6.8. If the blur induced by other components increases, the MTF decreases faster towards zero and the influence of the sampling aperture is less noticeable.

The pixel size of a radiography system is fixed. We can nevertheless simulate the effects different pixel sizes would have on the MTF. It is important to note, that the MTF evaluation program works with pixel values and does not need a specified pixel size to calculate the MTF values. The pixel size is only inserted as a scaling factor when plotting the results. Thus it is possible to predict the MTF for different pixel apertures. This is demonstrated in Fig. 6.9, where the same edge image was evaluated assuming pixel sizes of 0.1 mm, 0.16 mm, and 0.2 mm. As expected, the resolution over the whole frequency range is best for the smallest sampling aperture. Fig. 6.9 is also a good illustration of the reciprocity induced by the Fourier transform: Greater sampling distances in the spatial domain produce more closely spaced data points in the frequency domain and vice versa. In the Mathematica documentation A.1, the pixel size is denoted by the variable p (in mm). The default setting is 0.16 mm, which is the pixel size of the SIEMENS Axiom Multix M detector.

In 2.3.3, we derived the Nyquist frequency of a detector with 0.16 mm pixel spacing as $\xi_{Ny} = 1/2p = 3.125$ Lp/mm. For frequencies $\xi > \xi_{Ny}$, the sampling is less frequent than required to accurately detect these frequencies and they are aliased into lower spatial frequencies, creating a spurious MTF. A comparison between the analytical and the evaluated sampling

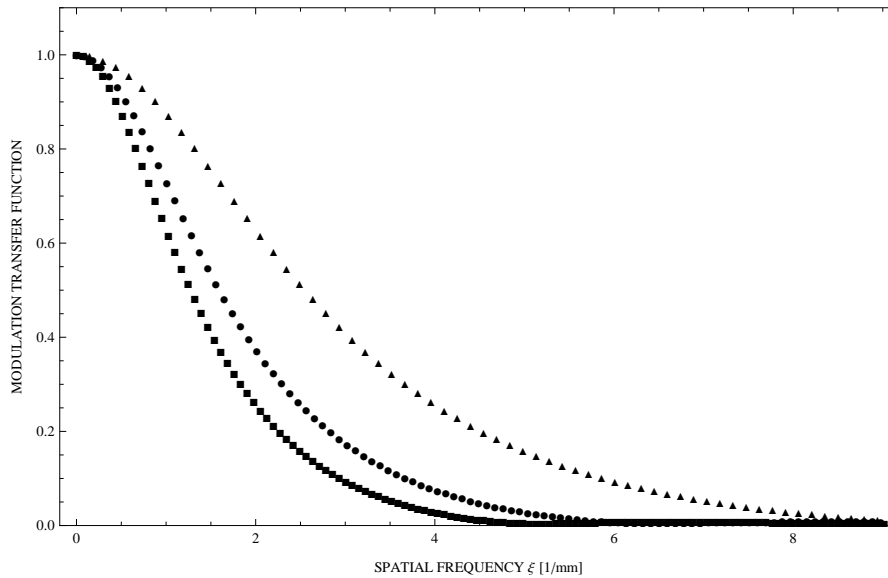


Figure 6.9.: MTFs calculated from the same edge image ($r = 1.8$, including sampling aperture) for different pixel dimensions. **Triangle:** 0.1 mm pixel spacing, **Circle:** 0.16 mm pixel spacing, **Square:** 0.2 mm pixel spacing.

MTF in Fig. 6.8 shows a perfect match. Aliasing effects are not visible to the naked eye. During the evaluation process, several lines of the edge image are interlaced, forming an oversampled ESF. For example, an edge angle of 1.9° results in an oversampling factor of $N_{int} = 30$. The Nyquist frequency for the oversampled ESF has shifted to $\xi_{Ny} = N_{int}/2p = 93.75 \text{ Lp/mm}$; a spatial frequency well beyond our area of inquiry. Both the calculation and the comparison of analytical and evaluated MTF show, that the interlacing of several lines to form the ESF effectively produces a presampled MTF without aliasing effects.

6.4. Motion Blur

With the method discussed in 2.3.4, we are able to calculate the MTF component for any motion function. A useful starting point for modeling patient movements is uniform linear motion. In real time imaging, uniform linear motion is assumed wherever motion is considered. Because of the short exposure duration (around 1/30 s), there is hardly any change in velocity during the exposure [YK97]. In radiography, the exposure duration is even shorter, being in the order of milliseconds.

We will therefore discuss the effects of uniform linear motion in detail and analyze its influence compared to other resolution limiting factors. We will also present several restoration techniques for motion-blurred images and use the MTF for test purposes to evaluate how precisely the initial image is restored. In the simulation of motion-blurred images, we will always include the influence of the sampling aperture. This is necessary for a realistic simulation, as sampling is omnipresent in digital images. The restoration algorithms for motion-blurred images are developed for digital images consisting of pixel arrays. Therefore, they can at best restore the image so that it equals that of an unmoving object. The image will still contain the resolution loss induced by the sampling aperture.

6.4.1. Implementing uniform linear motion

The MTF for uniform linear motion was derived analytically in 2.3.4. We recall the result as

$$\text{MTF}(\omega) = |\text{OTF}(\omega)| = \left| \text{sinc} \left(\frac{d}{2} \omega \right) \right| = |\text{sinc}(\pi d \xi)|, \quad (6.10)$$

with the blur extent d as the product of velocity v and exposure duration τ . To calculate the blur in the spatial domain, which is necessary for the generation of a simulation image, we perform a Fourier transform of (6.10) and obtain the PSF of uniform linear motion

$$\text{PSF}(x) = \Pi \left(\frac{x}{d} \right) = \Pi \left(\frac{x}{v\tau} \right). \quad (6.11)$$

We observe that the implementation is similar to that of the sampling aperture. A velocity of v perpendicular to the edge during the exposure duration τ induces a one-dimensional blur over the length $d = v\tau$. The result is a rectangular function of width d .

For the calculation of a simulation image which includes both effects from the sampling aperture and from uniform linear motion, the standard edge response ESF_{sim} (6.1) is convoluted with the sampling PSF in (6.9) (with $a = p$ and $y = 0$) and the motion PSF in (6.11). As before, the Mathematica documentation works on a pixel level. Therefore, we set $a = 1$ and express d as a multiple of the pixel size p .

Our results so far enable us to map the gradual loss of resolution induced by the sampling aperture and uniform linear motion of different velocities (Fig. 6.10). For this purpose, several simulation images were generated. The standard edge transition was set via $r = 1.8$ for all images. One image had a PSF that consisted solely of this standard transition. Another

one was additionally convoluted with the PSF of the sampling aperture. The last three were not only convoluted with the sampling PSF but also with individual motion PSFs which included three different velocities v_1 , v_2 and v_3 (for fixed exposure duration), corresponding to motion blurs with extents of 1 px, 2 px and 3 px, respectively. The simulation images were evaluated with the MTF program, where p was once more set to be 0.16 mm. The velocities depend on the exposure duration; for example, for $\tau = 20$ ms we would have $v_1 = 0.8$ cm/s, $v_2 = 1.6$ cm/s, and $v_3 = 2.4$ cm/s. The analytical expressions for the various MTFs were calculated by multiplying the individual MTF components. They are plotted alongside the discrete MTFs from the evaluation program to verify the correspondence between convolution of the PSFs in the spatial domain and multiplication of the MTFs in the spatial frequency domain. Naturally, the resolution decreases with higher velocity.

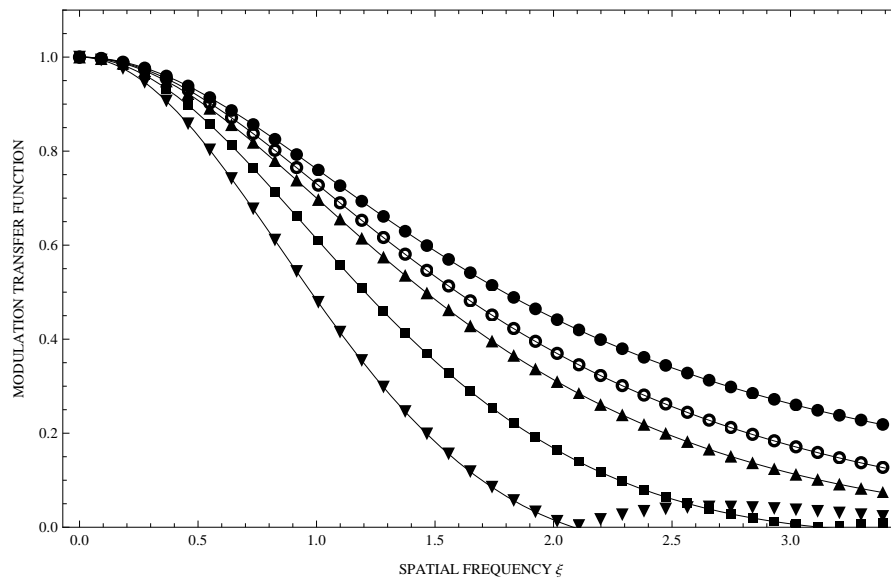


Figure 6.10.: Blur with $r = 1.8$, additional sampling ($p = 0.16$ mm), additional velocity 1 px blur, 2 px blur and 3 px blur. Discrete data from evaluation program and analytical MTFs.

6.4.2. Interaction between sampling aperture and motion

The degrading influence of object motion decreases for lower velocities. Bearing in mind that any image suffers from resolution loss due to the sampling aperture, the question arises whether there exists a limit velocity below which the motion blur goes unnoticed because of other resolution limiting factors.

To answer this question, we examine the convolution of the impulse responses for sampling and object motion in the spatial domain. Both PSFs have a rectangular pulse form. We express the impulse responses in terms of pixels, so that they correspond with their implementation in the Mathematica documentation A.3.4. Therefore, we set $p = 1$ and express d in multiples of

p. The sampling PSF has the width of 1 and an amplitude of 1 (Fig. 6.11a). The width of the motion PSF is the extent d of the motion blur, its amplitude is $1/d$ (Fig. 6.11b). The convolution of both pulses produces the pattern shown in Fig. 6.11c. It consists of two sloping lines and a flat spot. The flat spot has a width equal to the difference between the two pulse widths, $|d - 1|$. The width of the nonzero part of the function is the sum between the two pulse widths, $d + 1$. The slope of the intermediate lines depends on the amplitude of the pulses and has a value of $\frac{2}{d}(d + 1 - |d - 1|)^{-1}$. This leads to the following results: In the

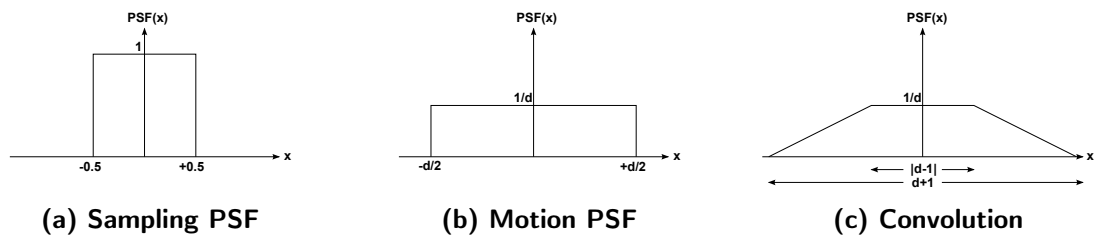


Figure 6.11.: Convolution of sampling and motion PSFs.

special case where the blur extent is exactly the size of one pixel, the pulse has a triangular shape instead of a flat spot. The first zero of the motion and the sampling MTF fall together and form the first zero of the overall MTF. Over the whole frequency range, the overall MTF is lower than the MTFs for sampling and motion alone. In all other cases, the pulse has the trapezoid form as in Fig. 6.11c. If the motion blur is greater than the pixel size ($d > p$), the first zero of the overall MTF is determined by the first zero of the motion MTF at $\xi = 1/d$. The overall MTF is overall lower than the MTF for motion alone. If the motion blur is less than the pixel size, the influence of the sampling PSF dominates and the first zero of the MTF occurs at $\xi = 1/p$. The overall MTF is lower than the MTF for sampling alone. For very small motion blurs, the pulse shape increasingly resembles that of a rectangular pulse. However, only for zero velocity does the convolution exactly reproduce the rectangular function of the sampling aperture. We conclude that there does not exist a limit velocity below which object motion has no degrading influence on the image. Object motion at any velocity introduces a resolution loss in the image. This is also valid in the presence of degrading mechanisms other than sampling.

An examination of the problem in the spatial frequency domain confirms our results (and once again demonstrates the simplicity of the calculations compared to the spatial domain). The overall MTF is formed by multiplication of the individual components of all resolution reducing mechanisms. Each component has a value below unity for all frequencies $\xi > 0$. Thus, every degrading mechanism has its share in the overall degradation and no component goes unnoticed.

6.4.3. Restoration of motion-blurred images

Transfer functions are tools to describe the influence of imaging components on the systems resolution. On the other hand, if the transfer function of a component is known, it is possible

to lessen the degrading influence of this component in the image. This is done by *deconvolution* of the image with PSF of the mechanism. Image deconvolution is able to reduce noise, sharpen or remove motion blur in an image. For Fig. 6.12a, a radiograph of a hand phantom was taken and blurred with a rectangular function of 3 px width along the horizontal axis to induce a motion blur. The image was then restored (Fig. 6.12b) using a total variation algorithm and the convolution kernel. Apparently, the motion blur in the restored image is reduced. What remains is the question: How well has the image been restored? To assess the effects of a restoration, in terms of both the discrepancy to the original image and the distinctions between several algorithms, we need an instrument with which the resolution can be quantified. The idea suggests itself to use the modulation transfer function for exactly this purpose.



(a) The CR image of a hand was blurred with an extent of 3 px.



(b) Image was restored with total variation regularization algorithm.

In this section, a short overview of restoration techniques is presented. It is followed by the implementation of selected algorithms and the associated MTF analysis. A detailed examination with the objective to find the best suited method to restore motion blur in radiographs would go well beyond the scope of this work. However, we will illustrate the usefulness of the MTF for the evaluation of restoration techniques and suggest methods which are later used for treatment of experimentally obtained radiographs.

We recall the situation in 2.2. The image $im(x, y)$ is generated by convolution of the object $obj(x, y)$ with the PSF of the system, which contains information about the system's performance in mathematical form. Our ambition is to calculate the original object function $obj(x, y)$ from the measured image $im(x, y)$ and the known PSF. While a convolution can always be calculated, deconvolution of two functions is analytically not feasible. The convolution process involves information loss, making deconvolution ill-posed. During the last 40 years, several computationally intensive algorithms have been developed, which are capable of approximately restoring the information content of the object. Based on the various

applications in astronomy, seismology, photography and various other areas, each algorithm has assets and drawbacks regarding the impact of noise, the computation time, preconditions and requirements.

A transfer into the spatial frequency domain further illustrates the problem statement. The frequency spectrum of the image $IM(\xi, \eta)$ is obtained by multiplying the frequency spectrum of the object $OBJ(\xi, \eta)$ with the optical transfer function:

$$IM(\xi, \eta) = OTF(\xi, \eta) \cdot OBJ(\xi, \eta) \quad (6.12)$$

In principle, the application of an *inverse filter*

$$M(\xi, \eta) = \frac{1}{OTF(\xi, \eta)} \quad (6.13)$$

would produce a frequency spectrum of the restored image $\widehat{OBJ}(\xi, \eta)$ equal to that of the original object, which could be Fourier transformed to yield the restored image $\widehat{obj}(x, y)$. This naive approach possesses several drawbacks. The most obvious is the requirement of a nonzero OTF for all frequencies, otherwise the expression in (6.13) is undefined. So far, each MTF for geometric unsharpness, sampling and motion featured an infinite number of zeros. Because of the finite size of the aperture, both the PSF and the measured image are band-limited, contrary to the object. Furthermore, every experimentally obtained image will feature a certain amount of noise. Application of an inverse filter would enhance the noise level, as the noise frequency spectrum $N(\xi, \eta)$ is increased for all frequencies

$$\widehat{OBJ}(\xi, \eta) = OBJ(\xi, \eta) + \frac{N(\xi, \eta)}{OTF(\xi, \eta)}. \quad (6.14)$$

Spectral deconvolution Provided that the power spectral density of the object $S_{oo}(\xi, \eta)$ and the mean power spectral density of the noise $S_{nn}(\xi, \eta)$ is known, the inverse filter (6.13) can be modified to minimize the influence of deconvoluted noise, especially for images with low SNR. An example of this technique is the *Wiener filter* [Wie70]:

$$M(\xi, \eta) = \frac{1}{OTF(\xi, \eta)} = \frac{|OTF(\xi, \eta)|^2}{|OTF(\xi, \eta)|^2 + \frac{S_{nn}(\xi, \eta)}{S_{oo}(\xi, \eta)}}. \quad (6.15)$$

The main advantage of spectral deconvolution methods is the short computer run-time. However, they require the knowledge of the spectral density of the object, which is generally unknown [Kop98]. The methods thus work with an assumed spectral density, which produces perfect results in some cases, and perfect nonsense in others.

Iterative deconvolution Iterative deconvolution techniques are nonlinear and therefore generally more effective than the simple linear spectral filtering techniques. They are widely used in astronomy, medical tomography and satellite sensors. As an iterative algorithm, the deconvolution is based on the result of the previous iteration, and the potentially slow

convergence implies considerable computational requirements [BA97]. The most popular iterative technique for deconvolution is the *Richardson-Lucy restoration algorithm*, which attempts to maximize the likelihood of the restored imaging by means of the expectation-maximization algorithm [Luc74, Ric72]. It is optimized for image systems under the influence of Poisson noise, and therefore most interesting for radiography. The algorithm can be expressed as

$$\widehat{\text{obj}}_{k+1}(x, y) = \widehat{\text{obj}}_k(x, y) \left(\text{PSF}(x, y) \star \frac{\text{im}(x, y)}{\text{PSF}(x, y) \star \widehat{\text{obj}}_k(x, y)} \right), \quad (6.16)$$

where $\widehat{\text{obj}}_k$ is the k -th estimate of the object and \star denotes the correlation operator. The denominator $\text{PSF} \star \widehat{\text{obj}}$ contains the estimated object convoluted with the PSF. The comparison of this so-called "reblurred" image with the measured image controls the iteration. The Richardson-Lucy algorithm requires a good estimate of the PSF to provide adequate results. Conservation of energy and non-negativity are maintained. Conservation of energy is maintained between the measured and the restored image (i.e. the total number of photons does not change), as well as non-negativity (i.e. the photon count is not negative) [BA97].

Iterative total variation regularization algorithm Since its first suggestion in 1992 [ROF92], total variation regularization has rapidly developed into one of the most important methods for noise removal, but it can also be used for image deconvolution with a known PSF. The main idea is that any signal (or image) with excessive noise or spurious detail has a high total variation

$$\text{TV}(\text{im}(x, y)) = \int |\nabla \text{im}(x, y)| dx dy. \quad (6.17)$$

Reduction of the total variation will remove unwanted detail, but preserve the important detail, such as edges. This explains its triumph over simple filtering or smoothing techniques, which remove important features along with the noise. The method allows the implementation of several noise models and offers a regularization parameter that determines the balance between goodness of fit to the measured data and the amount of regularization done to the measured data $\text{im}(x, y)$ in order to produce $\widehat{\text{obj}}(x, y)$ [SC03].

To apply any of the above mentioned techniques to digital images, the algorithms need to be discretized, and thus approximated. This implies that the algorithms can only restore images until the sampling stage, as already mentioned above.

We will now illustrate the effects of three different restoration algorithms on a motion blurred image. The MTF of the motion blurred image contains the blur of the standard edge transition (6.3) at $r = 1.8$, along with influences from the sampling aperture ($p=0.16$ mm) and a motion blur of 3 px width perpendicular to the edge. The discrete MTF from evaluation of the unrestored image takes exactly this shape (Fig. 6.13a). It is compared against the MTFs of

the images which were restored with a Wiener filter (Fig. 6.13b), a Richardson-Lucy algorithm (Fig. 6.13c) and a total variation regularization algorithm (Fig. 6.13d). Alongside the evaluated discrete MTF, each plot contains both the MTF including standard blur and sampling, and the MTF including standard blur, sampling and motion. This way, the restoration effects from the motion blurred image to the perfectly restored image can be easily interpreted. The various restorations were performed with Mathematica routines, the controllable parameters for the individual algorithms were chosen in such a way that the MTF was maximized. The MTFs were plotted up until the first zero of the sampling MTF at 6.25 lp/mm.

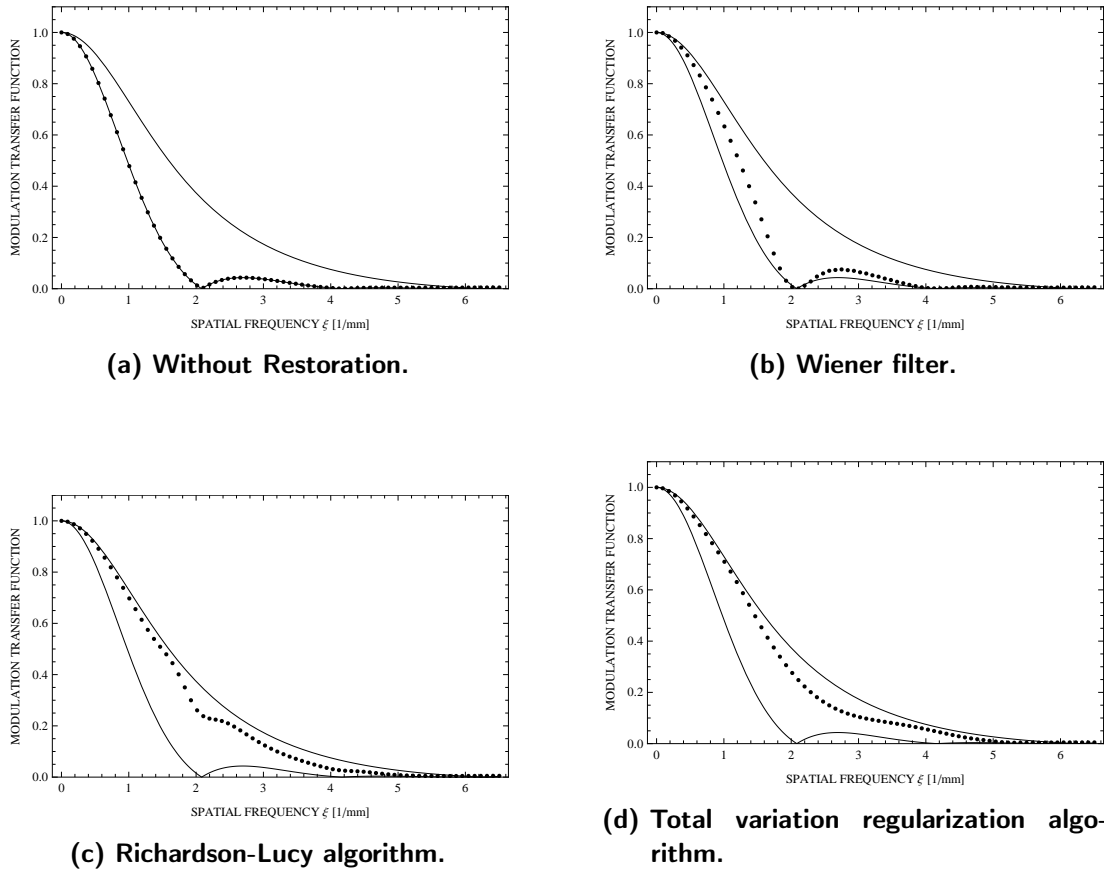


Figure 6.13.: Comparison of the performance of three restoration algorithms for a motion blurred image by means of the MTF. Continuous curves show MTF including standard blur ($r = 1.8$) and sampling (above) and MTF including standard blur ($r = 1.8$), sampling and 3 px motion blur (below).

As expected, the Wiener filter provides the smallest amount of restoration. The zeros of the motion MTF at multiples of $\xi = 1/d = 2.081/\text{mm}$ were not compensated, due to the singularities of the filter at these frequencies. Apart from the zeros, the MTF values were increased for all frequencies.

The Richardson-Lucy algorithm produced a discrete MTF with values close to the optimum

MTF. We observe the deviations around the zeros in the motion MTF. MTF values of frequencies $\xi > 1/d$ have absolutely as well as relatively greater deviations from the optimum than frequencies $\xi < 1/d$.

The total variation regularization equally produces a deviation around $\xi = 1/d$. Compared to the Richardson-Lucy algorithm, it extends over a broader spatial frequency range and the maximum deviation is not exactly at $\xi = 1/d$ but shifted somewhat to the right. On the other hand, the MTF for frequencies greater than 4 lp/mm is as close to the optimum as it is for low frequencies.

All methods produce acceptably smooth curves.

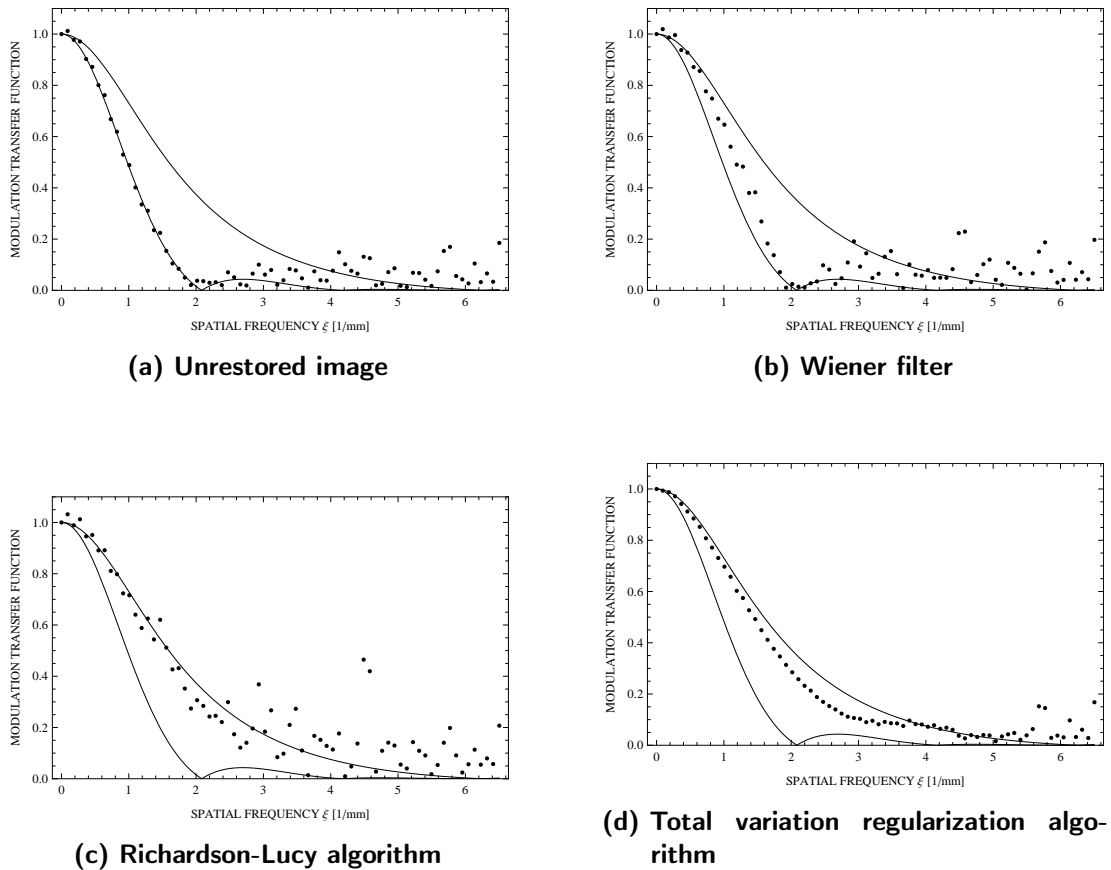


Figure 6.14.: Comparison of the performance of three restoration algorithms for a motion blurred image in the presence of Poisson noise by means of the MTF. Continuous curves show MTF including standard blur ($r = 1.8$) and sampling (above) and MTF including standard blur ($r = 1.8$), sampling and 3px motion blur (below).

The same procedure is now performed for a motion-blurred image which is additionally corrupted by Poisson noise. In doing so, we produce simulation images in high agreement with

experimental images from a radiography system. The Poisson noise was added to the image in the same way as described in 6.2.

The Wiener filter (Fig. 6.14b) once again suffers from the singularity at $\xi = 1/d$. We observe though, that the noise level is apparently not much higher than in the unrestored image. This means, that the noise is only slightly enhanced during the restoration process.

The greatest contrast between the restoration of the noiseless and the noisy image is seen with the Richardson-Lucy algorithm (Fig. 6.14c). The average of the MTF values up until around $\xi = 1/d$ corresponds to the MTF of the noiseless image. However, the overall noise level is extremely high and the enhancement of noise by the algorithm can be observed in particular around the second zero of the motion MTF at $\xi = 2/d = 4.2 \text{ lp/mm}$. Although in the literature the Richardson-Lucy algorithm is described as well-defined in the presence of Poisson noise, the results leave a lot to be desired.

Compared to these performances, it is astonishing, how the total variation regularization algorithm produces a MTF so smooth, that one can wonder whether any noise was present at all (Fig. 6.14d). Up until 3 lp/mm , the MTF values are equal to those obtained from the noiseless image. For higher spatial frequencies, we notice deviations and the onset of noise, increasing with frequency. Clearly, the total variation regularization algorithm outperforms the two other methods, as it not only effectively shifts the MTF towards the optimum but also drastically reduces the noise level without spoiling the curve shape.

Note that the algorithms work with discrete PSFs. While the simulation images in A.3.4 can be created with arbitrary motion blur, the width of the rectangular PSF inserted into the deconvolution must be expressed in multiples of one pixel. Restoration of other motion blur extents would require appropriate preprocessing of the image.

7. Results from Experiments

Now that we have a better understanding of the evaluation program, we complete our survey by adding some results from experimentally obtained images. The measurement method was described in a general form in 4. The particulars vary with the task, they are specified in the individual sections. To ensure that the edge angle lies approximately between 1.5° and 3° , every image was taken five times in a row while the edge device was slightly shifted in between exposures. The images were processed according to 5, noise reduction was applied via the averaging of several ESFs as described in 6.2.2. By reason of differing objectives and differing measurement methods, these experimental results are not directly comparable to other MTF measurements in the literature, as explained in 4.

After measurement of the detector MTF, geometric unsharpness was introduced by increasing the distance between detector and edge device. Subsequently, the edge device was mounted on the motion table and moved perpendicular to the edge with different velocities. The MTFs resulting from these measurements are presented, followed by a suggestion on how to reduce the motion blur via restoration.

As an optical guidance, the analytical MTF for the standard blur and a sampling aperture of $p = 0.16$ mm was compared to the measured detector MTF. The value of r was adapted to the course of the detector MTF for the relevant spatial frequency range. This analytical MTF does not contain valid information about the system. It is an estimate of the detector MTF which allows us to predict the influences of MTF components such as geometric unsharpness and motion. Note therefore, that the analytical MTFs in all following figures do not result from calculations, but depict the closest fit of the simulation MTF to the discrete MTF of the detector. They will be referred to as "estimated MTFs". Insertion of this curve into the plots of the discrete MTFs offers a comfortable comparison to the detector MTF and allows predictions about the influences of various components.

Note also that the differing spacing of the data points is not an indication of unequal imaging conditions, but results from the differing edge angles and image sizes. We recall that a smaller edge angle produces a greater subsampling factor, which after Fourier transform results in smaller spacings of the MTF data points. Reduction of the image size increases the spacings.

7.1. Detector Response

To measure the detector MTF, the edge device was positioned perpendicular to the incident x-ray beam at the center of the detector with a small angle between the detector array and the

edge of the device. The measurement was performed both in horizontal and vertical direction, i.e. with the edge aligned to the columns and rows of the detector array, respectively. The edge angle was $\alpha = 2.51^\circ$ in vertical direction and $\alpha = 2.89^\circ$ in horizontal direction. From Figs. 7.1a, 7.1b we see that the detector response slightly depends on the direction. This may be attributed to the spatial structures of the detector elements. For both images, seven data sets were used to produce an averaged ESF with reduced noise level. Nevertheless, the noise level is apparently greater in the horizontal direction. We do not observe a low frequency drop. As explained in 4.2, this is probably due to the limited suitability of the edge device. Both figures feature the estimated MTF mentioned above. The MTF was fitted to the detector MTF in vertical direction in the spatial frequency range $0 \text{ lp/mm} < \xi < 6 \text{ lp/mm}$, the corresponding value was $r=2.7$.

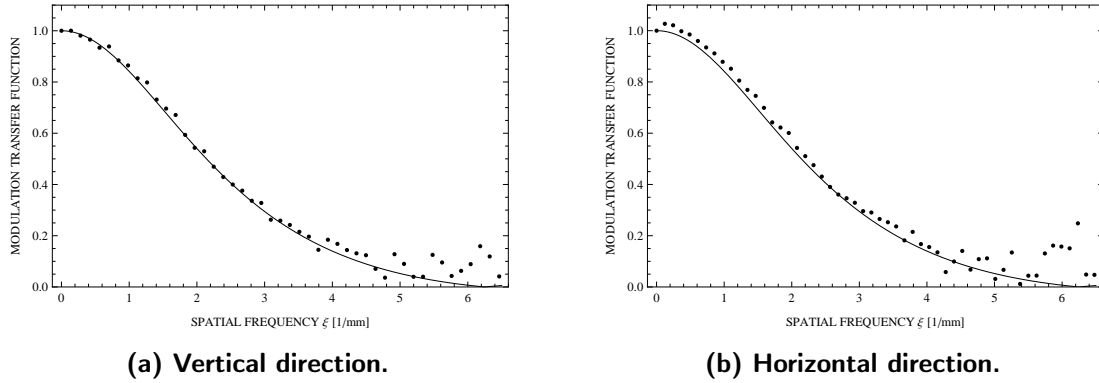


Figure 7.1.: Detector response of the Siemens Axiom Multix M (data points). Discrete MTFs from measurement in vertical and horizontal direction, along with estimated MTF which was fitted to the MTF in vertical direction (continuous line).

7.2. Geometric Unsharpness

The edge device was positioned perpendicular to the x-ray beam in distances of $d_2 = 10 \text{ cm}$ / $d_2 = 20 \text{ cm}$ from the detector. The measurement was conducted in vertical direction only. The edge angle was $\alpha = 1.34^\circ$ for $d_2=10 \text{ cm}$ and $\alpha = 1.65^\circ$ for $d_2 = 20 \text{ cm}$. Additionally to the estimated MTF of the detector, we include the influence of geometric unsharpness by multiplying the estimated MTF with the appropriate component derived in (2.21). The width of the penumbra is

$$U_g = f \frac{d_2}{d_1}, \quad (7.1)$$

with the focal spot size $f = 0.6 \text{ mm}$, the distance $d_1=115 \text{ cm}$ / $d_1=105 \text{ cm}$ between x-ray source and edge device and the distance $d_2 = 10 \text{ cm}$ / $d_2 = 20 \text{ cm}$ between edge device and detector.

Due to the small edge angle for $d_2 = 10$ cm, only three data sets could be used for averaging of the ESF. The MTF in (a) is therefore noisier than in (b), where seven sets were used for averaging.

We observe that the degradation of the MTF is only partially caused by geometric unsharpness, as the data points are considerably lower than the estimated curve. It is likely that x-ray scattering is responsible for the degradation.

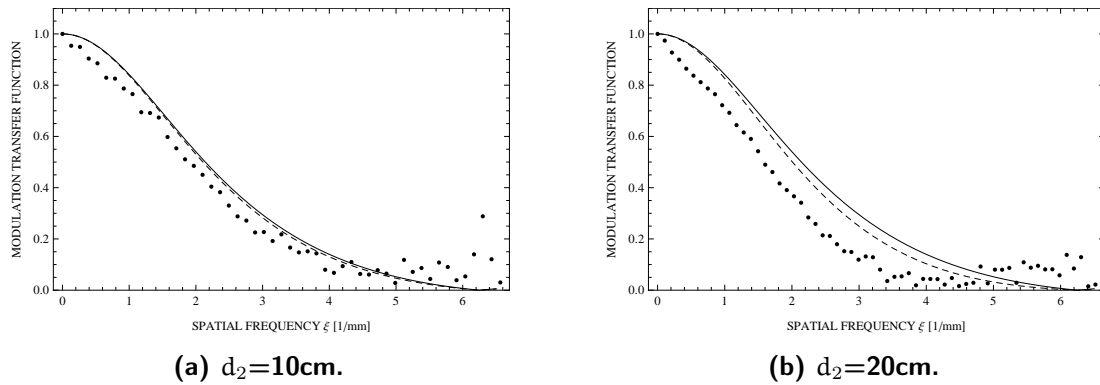


Figure 7.2.: MTFs of the Siemens Axiom Multix M measured 10 cm (a) and 20 cm (b) from the detector surface (data points), along with estimated MTF of the detector (continuous line) and estimated MTF of the detector including the influence of geometrical unsharpness (dashed line). Apparently, scattering effects have a greater influence on the MTF than geometric unsharpness.

7.3. Motion Blur

For measurement of the influence of uniform linear motion on the MTF, the edge device was mounted on the MotionSim table and moved with constant velocity over the center of the detector. The distance between edge device and detector was 11.5 cm. To analyze the motion influence, the MTF was first of all calculated from the image of the unmoving edge device. It is illustrated in Fig. 7.3. We see a degradation similar to those in the last section (Fig. 7.2a,7.2b). The estimated MTF of the detector ($r = 2.7$, dashed line) cannot offer a good comparison between motion MTFs with different velocities. We substitute it with a better fitting estimate ($r = 2.1$, continuous line). This estimate will be plotted alongside the discrete MTFs and the expected motion influence is calculated by multiplication of the estimated MTF with the appropriate sinc function (6.10). The blur extent $d = v \cdot \tau$ is calculated from the programmed velocity of the motion table and the exposure duration set by the radiography system.

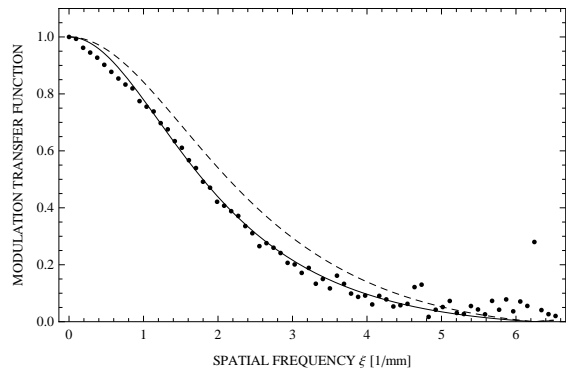


Figure 7.3.: MTF obtained by imaging edge device in a distance of 11.5 cm from the detector surface (height of motion simulator). Original fit of the standard blur(dashed line, $r = 2.7$), and new fit (continuous line, $r = 2.1$, better suited for additional degradation by scattering).

The first image was taken with an exposure duration of 5 ms and a velocity of 3.2 cm/s, which yields a motion blur extent of exactly $1 \text{ px} = 0.16 \text{ mm}$. The second image was taken with an exposure duration of 6 ms and a velocity of 5.08 cm/s (maximum velocity), causing a blur extent of $1.9 \text{ px} = 3.05 \text{ mm}$. Fig. 7.4 compares the MTF of the unmoved device and its analytical estimate to the MTFs including the above described motion blurs and their calculated estimates.

We observe that the discrete MTF for 1 px motion blur fits well to the estimated curve. For the 2 px blur, the actual degradation in the MTF is greater than the calculation of the estimated MTF foresees. As the form of the estimated curve fits the data points quite well, we can assume that the reason lies not in a badly fitted estimate of the MTF for the unmoved device, but that the blur extent used in the calculation must be faulty. This is supported by the fact that the first zero of the discrete MTF and the estimated MTF do not coincide. A possible explanation is the imprecisely known exposure duration, because the radiography system displays the duration in milliseconds, inducing a possible rounding error of $\pm 0.5 \%$, which has great influence on the position of the zeros in the MTF.

One can also see that although a noise reduction was employed, both MTFs are gravely corrupted by noise for frequencies above 4.5 lp/mm. Note that the sampling aperture forces the MTF to drop to zero at 6.25 lp/mm.

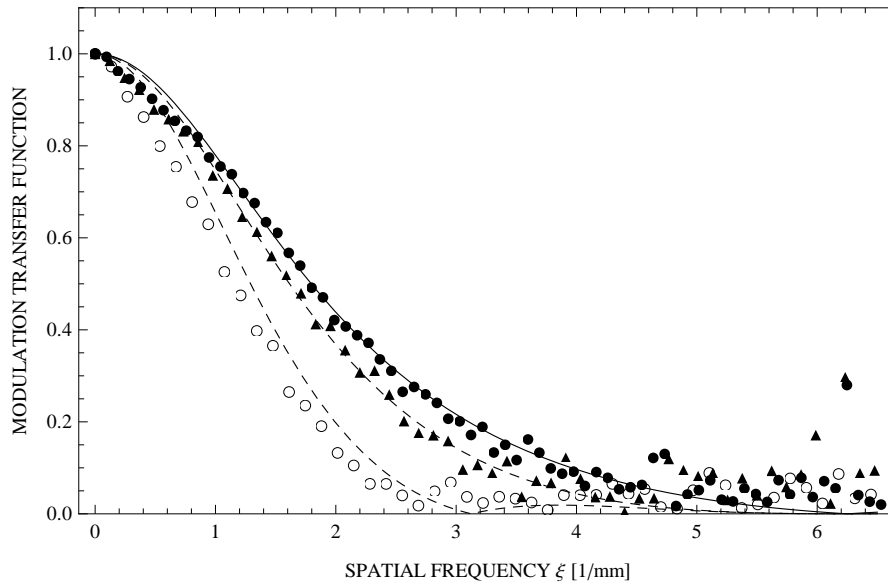
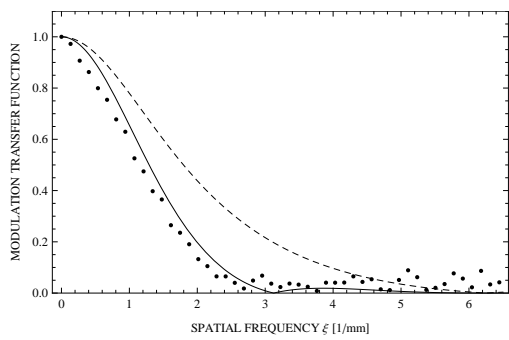


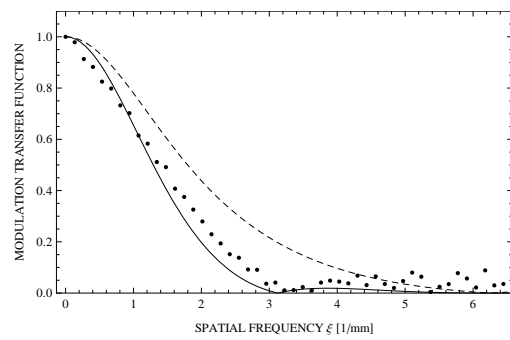
Figure 7.4.: Disks: MTF of the unmoved edge device in a distance of 11.5 cm from the detector surface; Triangles: MTF further including motion blur of 1 px extent; Circles: MTF further including motion blur of 1.9 px extent. Estimated MTF for the unmoved object ($r = 2.1$, continuous line) and modified for uniform linear motion of 1 px blur (above) and 2 px blur (below). The blur extent of 1.9 px is obviously faulty, probably due to a rounding error of the exposure duration.

7.4. Restoration

Finally, as a promising last result, we take the experimental image with 1.9 px motion blur extent in 7.3 and restore it with a total variation regularization algorithm. The routine 'ImageDeconvolve' in Mathematica demands a convolution kernel, that is to say, a PSF, of a blur extent which is a multiple of one pixel. We thus assume a PSF of 2 px width, which is the closest match. With the evaluation program at hand, we calculate the MTFs for both the original and the restored image and in both cases perform a noise reduction using five data sets. The results are shown in Figs. 7.5a and 7.5b. The first zero in the MTF has been immensely shifted from 2.71/mm to 3.31/mm. Especially in the mid-frequency range, the increase in the MTF is considerable. For lower frequencies, the amplitude gain decreases, but remains present and visible to the naked eye up unto the last data point. A decrease of the noise level as observed in 6.4.3 has not taken place. Considering that the convolution kernel was badly chosen in the first place, this outcome is very promising for future research in this area. One can imagine that the MTF could benefit still more from restoration, if an adequate blur extent was chosen as convolution kernel.



(a) Original Image.



(b) After Restoration.

Figure 7.5.: MTF of a motion blurred edge image ($d = 1.9$) and MTF of the same image after restoration with a total variation regularization algorithm. Continuous lines indicate the estimated MTF after restoration. The first zero in the MTF is shifted 0.6 1/mm to the right. The MTF values have increased for all frequencies, but especially for midrange frequencies.

8. Conclusion

In this thesis, the modulation transfer function (MTF) of a digital radiography system was examined. The individual components which reduce resolution were analyzed in terms of frequency response.

An analysis technique was presented which calculates the discrete MTF from an experimentally obtained or simulated edge image. With the evaluation program, the MTF of an arbitrary edge image can be calculated in practically no time with high accuracy.

The results showed that noise reduction via averaging of several ESF representations is highly commendable before further evaluation and should be performed with as many representations of the ESF as possible with regards to the image size.

The evaluation program was used to determine the detector response of the Siemens Axiom Multix MT radiography system. A combined use of the program with adaptable simulation images showed, that the MTF of an edge image obtained in a certain height above the detector is more strongly degraded by scattering effects than by geometric unsharpness.

Special emphasis was placed on the influence of motion on the image resolution. The MTF for an arbitrary motion function was calculated using moments and the result for uniform linear motion was affirmed by evaluation of simulation images which had been convoluted with the motion PSF in the spatial domain. Several restoration algorithms were presented and examined with respect to their application in post-processing. The MTF of a motion blurred image was shown to have increased amplitude over the whole frequency range after restoration of the image with a convolution kernel which was not even perfectly matched to the motion function.

As the deconvolution algorithms restore images in the spatial domain, the MTF will hardly ever be used for the restoration process itself. Instead, the convolution kernel, i.e. the PSF, can be calculated directly from the motion function. However, for verification of the effects of image restoration and of course for general analysis of the system's performance, the MTF is a crucial criterion.

With regard to a potential clinical application, it would be useful to map patient movements (e.g. via motion sensors or video recording). This would serve as input data for the image reconstruction.

The reconstruction method itself needs further verification. While in our example the total variation regularization algorithm produced the best results, this is not necessarily the case for all motion functions and all clinical applications.

So far, the restoration was only performed for motion blurs with extents of multiples of one subsampling pixel. While we obtained promising results even in the assumption of an ill-fitting convolution kernel, much better results are to be expected if the restoration could process convolution kernels of arbitrary extents. A small improvement might be made by expansion of the image onto a subsampling grid (similar as performed for the interlacing of the ESF). The information of one pixel would be extended over several subsampling pixels without alteration of the overall information content. Thus, the PSF would still be discrete, but could be expressed in multiples of one subsampling pixel.

As the detector MTF varies with the direction, it might be interesting to observe the directionality of the motion MTF. Apart from differences in the spatial structure, one might observe effects due to the readout order of the detector array.

A. Mathematica code

A.1. MTF evaluation program

A.1.1. Preparation of the image data

For experimental images, the data array “a” is extracted from an image file.

For simulation images, “a” is set to be the data array “edge” of the simulation image.

```
a = Import[ ..., "Data"];  
a = edge;  
dim = Dimensions[a]  
length = Dimensions[a][[1]]
```

A.1.2. Determination of the edge angle

```
angle = Array[f, dim[[1]]];  
average50list = Array[f, dim[[1]]];  
For[i = 1, i < dim[[1]] + 1, i++,  
  linedata = a[[i]];  
  average50 = Min[linedata] + (Max[linedata] - Min[linedata]) / 2;  
  average50list[[i]] = average50;  
  line = Interpolation[linedata, InterpolationOrder -> 1];  
  sol = FindRoot[Evaluate[line][x] - average50, {x, 1, dim[[2]]}];  
  angle[[i]] = x /. sol;  
]  
sol = FindFit[angle, m * x + c, {m, c}, x]  
Res = Abs[ArcTan[m /. sol]] / Degree  
SamplingDirection = Sign[ArcTan[m /. sol]]  
NintAve = 1 / (m /. sol)  
Nint = Round[1 / (m /. sol)]
```

A.1.3. Construction of the oversampled ESF

```
laenge = dim[[2]] * Nint
```

“start” signifies the number of the first line used to build the oversampled ESF.

It is set to be in the central region of the image, but can be shifted if necessary.

```
start = Round[length / 2] - (Nint + Mod[Nint, 2]) / 2
```

```
start = start + 0;
```

```
ESF1 = Array[f, laenge];
```

```
If[SamplingDirection < 0,
```

```
  For[i = 1, i < laenge + 1, i++,
```

```
    ESF1[[laenge + 1 - i]] = a[[start + Mod[i, Nint, 1] - 1, Ceiling[i / Nint]]],
```

```
  For[i = 1, i < laenge + 1, i++,
```

```
    ESF1[[i]] = a[[start + Nint - Mod[i, Nint, 1] + 1, Ceiling[i / Nint]]];
```

p: pixel spacing of sampling grid in mm

s: pixel spacing of subsampling grid in mm

Default setting is p=0.16.

```
p = 4 / 25
```

```
s = p / Nint
```

If a noise reduction is performed via averaging of several ESFs,

“laenge” must be changed to the length of the averaged ESF

and “ESF” must be set as the averaged ESF instead of “ESF1”.

```
laenge = laenge;
```

```
ESF = Array[f, laenge];
```

```
ESF = ESF1;
```

A.1.4. Derivation of the oversampled LSF

```
LSF1 = ListConvolve[{1 / 2, 0, -1 / 2}, ESF];
```

A.1.5. Fourier transform to obtain the presampled MTF

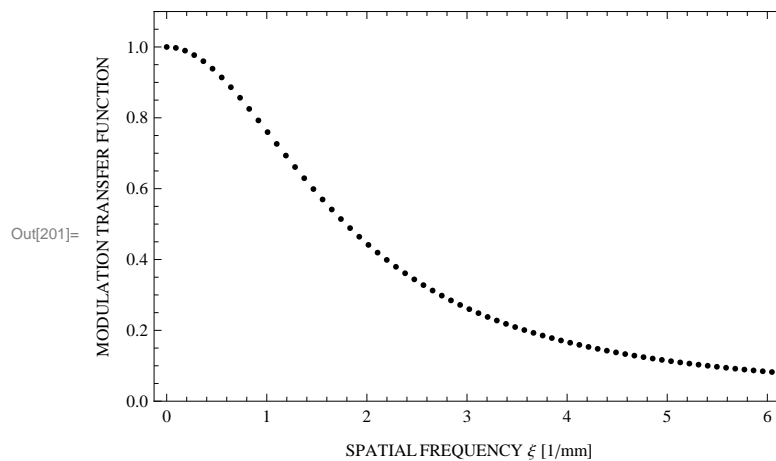
```
M = 2^Floor[Log[2, laenge]]
trunc = Ceiling[(laenge - M) / 2] // N
LSF = Array[f, M];
For[i = 1, i < M + 1, i++, LSF[[i]] = LSF1[[i + trunc]]]
MTF1 = Array[f, M];
MTF1 = Abs[Fourier[LSF, FourierParameters -> {-1, 1}]];
MTF2 = 1 / (MTF1[[1]]) * MTF1;
```

A.1.6. Corrections

```
In[202]:= MTFderiv[ξ_] = Sinc[2 π * ξ * 1];
MTF = Array[f, M];
For[i = 1, i < M + 1, i++, MTF[[i]] = MTF2[[i]] / MTFderiv[(i - 1) / M]]
```

Plot of the final result:

```
In[201]:= ListPlot[Table[{j / (M * s * Cos[Res / 360 * 2 π]), MTF[[j + 1]]},
  {j, 0, Round[6 * (M * s * Cos[Res / 360 * 2 π])]}],
  PlotRange -> {0, 1.1}, PlotStyle -> Black, Frame -> True,
  FrameLabel -> {"SPATIAL FREQUENCY ξ [1/mm]", "MODULATION TRANSFER FUNCTION"}]
```



A.2. Noise reduction

(exemplary for three data sets)

After determination of the edge angle and N_{int} , this code snippet is evaluated. In the MTF evaluation program “laenge” must be changed to “laenge3” and “ESF1” must be changed to “ESF3av” at the indicated positions.

```
laenge3 = laenge - 2 * Nint;
ESF = Array[f, laenge];
If[SamplingDirection < 0,
For[i = 1, i < laenge + 1, i++, ESF[[laenge + 1 - i]] =
  a[[start + Mod[i, Nint, 1] - 1, Ceiling[i / Nint]]], For[i = 1, i < laenge + 1,
  i++, ESF[[i]] = a[[start + Nint - Mod[i, Nint, 1] + 1, Ceiling[i / Nint]]]];
ESF02 = Array[f, laenge3];
For[i = 1, i < laenge3 + 1, i++, ESF02[[i]] = ESF[[i + Nint]]]
start = start - Nint;
If[SamplingDirection < 0,
For[i = 1, i < laenge + 1, i++, ESF[[laenge + 1 - i]] =
  a[[start + Mod[i, Nint, 1] - 1, Ceiling[i / Nint]]], For[i = 1, i < laenge + 1,
  i++, ESF[[i]] = a[[start + Nint - Mod[i, Nint, 1] + 1, Ceiling[i / Nint]]]];
ESF01 = Array[f, laenge3];
For[i = 1, i < laenge3 + 1, i++, ESF01[[i]] = ESF[[i]]]
start = start + 2 * Nint;
If[SamplingDirection < 0,
For[i = 1, i < laenge + 1, i++, ESF[[laenge + 1 - i]] =
  a[[start + Mod[i, Nint, 1] - 1, Ceiling[i / Nint]]], For[i = 1, i < laenge + 1,
  i++, ESF[[i]] = a[[start + Nint - Mod[i, Nint, 1] + 1, Ceiling[i / Nint]]]];
ESF03 = Array[f, laenge3];
For[i = 1, i < laenge3 + 1, i++, ESF03[[i]] = ESF[[i + 2 * Nint]]]
ESF3av = Array[f, laenge3];
For[i = 1, i < laenge3 + 1, i++, ESF3av[[i]] = 1 / 3 * (ESF01[[i]] + ESF02[[i]] + ESF03[[i]])]
```

A.3. Simulation images

A.3.1. Standard image

```
In[22]:= r = 1.8;
In[23]:=  $\beta = 1.9^\circ$ ;
In[24]:= edge = Array[f, {100, 100}];
In[25]:= esf = Piecewise[{{1 - 1/2 * Exp[-r * x], x >= 0}, {1/2 * Exp[r * x], x < 0}}];
In[27]:= For[j = 1, j < Dimensions[edge][[1]] + 1, j++, For[i = 1, i < Dimensions[edge][[2]] + 1,
    i++, edge[[j, i]] = esf /. {x -> i - Round[Dimensions[edge][[2]] / 2] - j * Tan[ $\beta$ ]}]]
```

A.3.2. Simulation image featuring Noise

```
r = 1.8;
 $\beta = 1.9^\circ$ ;
edgeN = Array[f, {100, 100}];
esf = Piecewise[{{1 - 1/2 * Exp[-r * x], x >= 0}, {1/2 * Exp[r * x], x < 0}}];
For[j = 1, j < Dimensions[edgeN][[1]] + 1, j++, For[i = 1, i < Dimensions[edgeN][[2]] + 1,
    i++, edgeN[[j, i]] = 1/1 * (esf /. {x -> i - Round[Dimensions[edgeN][[2]] / 2] - j * Tan[ $\beta$ ]}))
    + 1/100 * RandomInteger[PoissonDistribution[
        (esf /. {x -> i - Round[Dimensions[edgeN][[2]] / 2] - j * Tan[ $\beta$ ]})) + 0.15]]
    - 1/100 * RandomInteger[PoissonDistribution[
        (esf /. {x -> i - Round[Dimensions[edgeN][[2]] / 2] - j * Tan[ $\beta$ ]})) + 0.15]]]]
```

Change noise level via the ratio of the Poisson distribution. Default setting: 1/100.

A.3.3. Simulation image featuring Sampling

```
r = 1.8;
 $\beta = 1.9^\circ$ ;
edgeS = Array[f, {100, 100}];
esf[x_] = Piecewise[{{1 - 1/2 * Exp[-r * x], x >= 0}, {1/2 * Exp[r * x], x < 0}}];
aperture[x_] = UnitBox[x];
sample[y_] = Convolve[aperture[x], esf[x], x, y];
For[j = 1, j < Dimensions[edgeS][[1]] + 1, j++, For[i = 1, i < Dimensions[edgeS][[2]] + 1,
    i++, edgeS[[j, i]] = sample[i - Round[Dimensions[edgeS][[2]] / 2] - j * Tan[ $\beta$ ]]]]
```

A.3.4. Simulation image featuring Sampling and Object motion with/without Noise

```

r = 1.8;
β = 1.9 °;
esf[x_] = Piecewise[{{1 - 1 / 2 * Exp[-r * x], x >= 0}, {1 / 2 * Exp[r * x], x < 0}}];
aperture[x_] = UnitBox[x];

```

Motion Blur extent $d=(v*\tau)/p$, with v: velocity, τ : exposure duration, p: pixel spacing.

```

d = 3;
kernel[x_] = 1 / d * UnitBox[1 / d * x];
combo[y_] = Convolve[aperture[x], kernel[x], x, y];
samplemotion[y_] = Convolve[combo[x], esf[x], x, y];

```

Without Noise:

```

edgeSM = Array[f, {100, 100}];
For[j = 1, j < Dimensions[edgeSM][[1]] + 1, j++, For[i = 1, i < Dimensions[edgeSM][[2]] + 1,
  i++, edgeSM[[j, i]] = samplemotion[i - Round[Dimensions[edgeSM][[2]] / 2] - j * Tan[β]]]]

```

With Noise:

```

edgeSMN = Array[f, {100, 100}];
For[j = 1, j < Dimensions[edgeSMN][[1]] + 1,
  j++, For[i = 1, i < Dimensions[edgeSMN][[2]] + 1, i++,
    edgeSMN[[j, i]] = 1 / 1 * samplemotion[i - Round[Dimensions[edgeSMN][[2]] / 2] - j * Tan[β]] +
      1 / 100 * RandomInteger[PoissonDistribution[
        (samplemotion[i - Round[Dimensions[edgeSMN][[2]] / 2] - j * Tan[β]] + 0.15]]
      - 1 / 100 * RandomInteger[PoissonDistribution[
        (samplemotion[i - Round[Dimensions[edgeSMN][[2]] / 2] - j * Tan[β]] + 0.15]]]]]]

```

Bibliography

- [61205] IEC 61267:2005. *Medical diagnostic X-ray equipment - Radiation conditions for use in the determination of characteristics*. IEC, 2005.
- [62203] IEC 62220-1. *Medical Electrical Equipment - Characteristics of Digital X-ray Imaging Devices - Part 1: Determination of the Detective Quantum Efficiency*. IEC, 2003.
- [62205] DIN EN 62220-1:2005-1. *Medizinische elektrische Geräte - Merkmale digitaler Röntgenbildgeräte - Teil 1: Bestimmung der detektiven Quanten-Ausbeute (IEC 62220-1:2003); Deutsche Fassung EN 62220-1:2004*. Beuth Verlag, Berlin, 2005.
- [68692] DIN 6867-2:1992-11. *Bildregistrierendes System, bestehend aus Röntgenfilm, Verstärkungsfolien und Kassette zur Verwendung in der medizinischen Röntgen-diagnostik; Bestimmung der Modulationsübertragungsfunktion*. Beuth Verlag, Berlin, 1992.
- [BA97] David S C Biggs and Mark Andrews. Acceleration of iterative image restoration algorithms. *Applied Optics*, 36(8), 1997.
- [BGKN03] Egbert Buhr, Susanne Günther-Kofahl, and Ulrich Neitzel. Accuracy of a simple method for deriving the presampled modulation transfer function of a digital radiographic system from an edge image. *Medical Physics*, 30(9), 2003.
- [Boo01] John M Boone. Determination of the presampled mtf in computed tomography. *Medical Physics*, 18(3), 2001.
- [Bor01] Glenn D Boreman. *Modulation Transfer Function in Optical and Electro-Optical Systems*. SPIE Press, 2001.
- [BW99] Max Born and Emil Wolf. *Principles of optics*. Cambridge University Press, 1999.
- [CF87] I A Cunningham and A Fenster. A method for modulation transfer function determination from edge profiles with correction for finite-element differentiation. *Medical Physics*, 14(4), 1987.
- [CKS⁺08] Hyun Choi, Jong-Pil Kim, Myeong-Gyu Song, Wan-Chin Kim, No-Cheol Park, Young-Pil Park, and Kyoung-Su Park. Effects of motion of an imaging system and optical image stabilizer on the modulation transfer function. *Optics express*, 16(25), 2008.

- [Col54] John W Coltman. The specification of imaging properties by response to a sine wave input. *Journal of the Optical Society of America*, 44(6), 1954.
- [Com11a] DICOM Standards Committee. Digital imaging and communications in medicine (dicom), part 1: Introduction and overview, 2011.
- [Com11b] DICOM Standards Committee. Digital imaging and communications in medicine (dicom), part 10: Media storage and file format for media interchange, 2011.
- [Dös00] Olaf Dössel. *Bildgebende Verfahren in der Medizin*. Springer, 2000.
- [Fis82] M G Fisher. Mtf, noise power and DQE of radiographic screens. *Photographic Science and Engineering*, 26(1), 1982.
- [Fow75] Grant R Fowles. *Introduction to modern optics*. Dover Publications, 1975.
- [FTI⁺92] Hiroshi Fujita, Du-Yih Tsai, Takumi Itoh, Kunio Doi, Junji Morishita, Katsuhiko Ueda, and Akiyoshi Ohtsuka. A simple method for determining the modulation transfer function in digital radiography. *IEEE Transactions on Medical Imaging*, 11(1), 1992.
- [GD84] Maryellen L Giger and Kunio Doi. Investigation of basic imaging properties in digital radiography. i. modulation transfer function. *Medical Physics*, 11(3), 1984.
- [HDK94] Ofer Hadar, Itai Dror, and Norman S Kopeika. Image resolution limits resulting from mechanical vibrations: Part iv: real-time numerical calculation of optical transfer function and experimental verification. *Optical engineering*, 33, 1994.
- [iD13] Normenausschuss Radiologie (NAR) im DIN. Medical electrical equipment - characteristics of digital x-ray imaging devices - part 1: Determination of the detective quantum efficiency - detectors used in radiographic imaging, german version, 2013.
- [Kop98] Norman S Kopeika. *A System Engineering Approach to Imaging*. SPIE Press, 1998.
- [LR67] G Lubberts and L Rossmann. Modulation transfer function associated with geometrical unsharpness in medical radiography. *Physics in medicine and biology*, 12(1), 1967.
- [LT88] Fang Lei and H J Tiziani. A comparison of methods to measure the modulation transfer function of aerial survey lens systems from the image structures. *Photogrammetric Engineering and Remote Sensing*, 54(1), 1988.
- [Luc74] L B Lucy. An iterative technique for the rectification of observed images. *The Astronomical Journal*, 79(6), 1974.

- [LWS05] Wei Lin, Felix W Wehrli, and Hee Kwon Song. Correcting bulk in-plane motion artifacts in mri using the point spread function. *IEEE Transactions on Medical Imaging*, 24(9), 2005.
- [Mac83] Albert Macovski. *Medical imaging systems*. Prentice-Hall Englewood Cliffs, NJ, 1983.
- [Nil01] Norman B Nill. Conversion between sine wave and square wave spatial frequency response of an imaging system, 2001.
- [NMGK94] Ulrich Neitzel, Ingo Maack, and Susanne Günther-Kofahl. Image quality of a digital chest radiography system based on a selenium detector. *Medical Physics*, 21(4), 1994.
- [O'H91] Tom O'Haver. An introduction to signal processing in chemical measurement. *Chemical education*, 68(6), 1991.
- [Pap84] Athanasios Papoulis. *Probability, Random Variables, and Stochastic Processes*. McGraw-Hill, 1984.
- [Pel90] Eli Peli. Contrast in complex images. *Journal of the Optical Society of America A*, 7(10), 1990.
- [PIK92] John Princen, John Illingworth, and Josef Kittler. A formal definition of the hough transform: Properties and relationships. *Journal of Mathematical Imaging and Vision*, 1(2), 1992.
- [PL06] Jerry L Prince and Jonathan M Links. *Medical imaging signals and systems*. Prentice-Hall, 2006.
- [PSK84] Stephen K Park, Robert Schowengerdt, and Mary-Anne Kaczynski. Modulation-transfer-function analysis for sampled image systems. *Applied Optics*, 23(15), 1984.
- [PTVF07] William H Press, Saul A Teukolsky, William T Vetterling, and Brian P Flannery. *Numerical Recipes*. Cambridge University Press, third edition, 2007.
- [Ric72] William H Richardson. Bayesian-based iterative method of image restoration. *Journal of the Optical Society of America*, 62(1), 1972.
- [ROF92] Leonid I Rudin, Stanley Osher, and Emad Fatemi. Nonlinear total variation based noise removal algorithms. *Physica D*, 60, 1992.
- [RSIR05] Nicole T Ranger, Ehsan Samei, James T Dobbins III, and Carl E Ravin. Measurement of the detective quantum efficiency in digital detectors consistent with the IEC 62220-1 standard: Practical considerations regarding the choice of filter material. *Medical Physics*, 32(7), 2005.

- [SBG⁺05] Ehsan Samei, Egbert Buhr, Paul Granfors, Dirk Vandenbroucke, and Xiaohui Wang. Comparison of edge analysis techniques for the determination of the mtf of digital radiographic systems. *Physics in Medicine and Biology*, 50, 2005.
- [SC03] David Strong and Tony Chan. Edge-preserving and scale-dependent properties of total variation regularization. *Inverse Problems*, 19, 2003.
- [SFR98] Ehsan Samei, Michael J Flynn, and David A Reimann. A method for measuring the presampled mtf of digital radiographic systems using an edge test device. *Medical Physics*, 25(1), 1998.
- [SG64] Abraham Savitzky and Marcel JE Golay. Smoothing and differentiation of data by simplified least squares procedures. *Analytical chemistry*, 36(8), 1964.
- [SK97] A Stern and N Kopeika. Analytical method to calculate optical transfer functions for image motion and vibrations using moments. *Journal of the Optical Society of America A*, 14(2), 1997.
- [SRIC06] Ehsan Samei, Nicole T Ranger, James T Dobbins III, and Ying Chen. Intercomparison of methods for image quality characterization. I. modulation transfer function. *Medical Physics*, 33(5), 2006.
- [Tro60] T Trott. The effects of motion in resolution. *Photogrammetric Engineering*, 26, 1960.
- [Wie70] Norbert Wiener. *Extrapolation, interpolation, and smoothing of stationary time series*. M.I.T. Press, 1970.
- [Wil02] Charles S Williams. *Introduction to the optical transfer function*. SPIE Press, 2002.
- [Wim] Leonhard Wimmer. A siemens star, rendered as svg (created manually). Licensed under the Creative Commons Attribution-Share Alike 3.0 Unported license: <http://www.creativecommons.org/licenses/by-sa/3.0/legalcode>.
- [YK97] Yitzhak Yitzhaky and Norman S Kopeika. Identification of blur parameters from motion blurred images. *Graphical Models and Image Processing*, 59(5), 1997.

Acknowledgements

I would like to thank Dr. Andreas Block and Prof. Dr. Georg Pretzler for supervising the present thesis and giving support and helpful advice.

Moreover, I would like to express my thanks to Dr. Ulrich Neitzel, Dr. Helmuth Schramm, Isabel Weiß and Andreas Mewes for their detailed and constructive comments and technical assistance.

Eidesstattliche Erklärung

Eidesstattliche Erklärung gemäß §13 Abs. 11 der Prüfungsordnung für den Master-Studiengang Medizinische Physik an der Heinrich-Heine-Universität Düsseldorf.

Hiermit versichere ich an Eides statt, dass ich die vorliegende Masterarbeit selbstständig und ohne unzulässige fremde Hilfe erbracht habe. Ich habe keine anderen als die angegebenen Quellen und Hilfsmittel benutzt sowie wörtliche und sinngemäße Zitate kenntlich gemacht.

Diese Arbeit hat in gleicher oder ähnlicher Form noch keiner Prüfungsbehörde vorgelegen.

Arnsberg, den 31. Januar 2014

(Katharina Loot)